Revision 1 Word Count: 7926

Effect of pre-existing crystals and melt homogeneity on the decompression-induced crystallization of hydrous rhyodacite magma

Kazuhisa Matsumoto[1,2], Satoshi Okumura[1,2], and Akihiko Tomiya[2]

[1] Division of Earth and Planetary Materials Science, Department of Earth Science, Graduate School of Science, Tohoku University, 6-3 Aramaki Aza-Aoba, Aoba-ku, Sendai 980-8578 Miyagi, Japan

[2] Geological Survey of Japan, National Institute of Advanced Industrial Science and Technology

*Corresponding author

Kazuhisa Matsumoto

Division of Earth and Planetary Materials Science, Department of Earth Science, Graduate School of Science, Tohoku University, 6-3 Aramaki Aza-Aoba, Aoba-ku, Sendai 980-8578 Miyagi, Japan.

Tel&Fax +81-22-795-7764: Email kazuhisa.matsumoto.q6@dc.tohoku.ac.jp

Abstract

Decompression-induced crystallization is an important process that controls the behavior of volcanic eruptions because it strongly affects magma rheology and degassing behavior in the shallow parts of volcanic conduits. Several decompression experiments have been performed to understand and model the crystallization processes; however, the effect of superheating (i.e., heating above the liquidus temperature for a definite period of time) before decompression has not been elucidated, despite the proposal of its importance in previous cooling experiments. As the superheating influences the number of pre-existing crystals and melt homogeneity, it is expected to control decompression-induced crystallization. In this study, we investigated the effects of pre-existing crystals and melt homogeneity on crystallization during the decompression of rhyodacitic magma at a temperature of 900°C. The magma studied herein has a liquidus temperature of ~920°C. Five starting materials were prepared via heating at different super-liquidus temperatures (940, 970, 1050 and 1300°C) and a sub-liquidus temperature (900°C) using an internally heated pressure vessel and a cold-seal pressure vessel, respectively. Decompression experiments using these starting materials were conducted from 130 to 30 MPa at decompression rates of 5, 20, and 100 MPa h^{-1}. When the melt was completely homogenized (at 1050 and 1300°C), no crystals were formed at 100 MPa h^{-1} and the small amounts of crystals heterogeneously formed along the capsule wall were found at 5 and 20 MPa h^{-1}. At the same decompression rate, the number density of plagioclase formed during decompression increased as the superheating temperature decreased from 970 to 900°C, despite the higher number densities of pre-existing crystals before decompression in the samples with lower superheating. Such finding indicates that nucleation occurs easily when the number density is initially high. This result is inconsistent with the idea that nucleation occurs when supersaturation is sufficient to overcome the energy barrier for nucleation, and the growth of pre-existing crystals decreases supersaturation. In contrast, the results of our experiments can be explained by considering that higher superheating results in a more homogeneous melt structure with few pre-crystal clusters, which are growth sites, and ultimately the suppression of nucleation. Based on these results, we conclude that pre-existing crystals and melt homogeneity strongly affect the crystal texture formed by decompression. For application to natural systems, the high number density of microlites found in natural samples may be due to heterogeneous nucleation caused by the presence of pre-crystal clusters and other mechanisms. Furthermore, the superheating of magma in a reservoir caused by the injection of high-temperature mafic magma may influence the crystal texture during magma ascent and, hence, control the explosivity of the eruption.

Keywords: Decompression-induced crystallization, superheating, magma decompression, crystal texture

INTRODUCTION

Decompression during magma ascent to the surface causes dehydration and hence changes in the liquidus of hydrous magma, resulting in crystallization (Cashman, 1992; Hammer and Rutherford, 2002). Decompression-induced crystallization strongly controls eruption dynamics because it causes an increase in the magma viscosity (Melnik and Sparks, 1999; Gonnermann and Manga, 2003). The number density of crystals and total crystallinity of natural samples that experienced decompression-induced crystallization have been used to estimate the decompression rate using experimentally calibrated theories (Toramaru et al., 2008). To this end, several experimental studies have been performed to determine the relationship between the decompression history and crystal texture (e.g., Hammer and Rutherford, 2002; Couch et al., 2003a, 2003b; Martel and Schmidt, 2003; Brugger and Hammer, 2010; Cichy et al., 2011; Mollard et al., 2012; Shea and Hammer, 2013; Fiege et al., 2015; Riker et al., 2015; Befus and Andrews, 2018; Lindoo and Cashman, 2021).

Based on previous studies, the decompression history, such as decompression rate, final pressure, and decompression paths (i.e., single-step, multi-step, or continuous decompression) has been recognized to affect the number density of crystals formed during decompression. A high decompression rate results in a large undercooling; hence, the number density of the microlite formed during decompression becomes large (e.g., Couch et al., 2003b; Shea and Hammer, 2013). Additionally, Brugger and Hammer (2010) demonstrated that the number density of plagioclase microlites formed during continuous decompression is higher than that of microlites formed by multi-step decompression.

In addition to the decompression history, the condition before decompression is an important factor that determines the crystal texture after decompression. In nature, the magma in the reservoir contains crystals (phenocrysts) and can be heated and cooled by magma injection into the reservoir in the cold crust (e.g., Kent et al., 2010; Tomiya et al., 2013; Cooper and Kent, 2014). As the temperature of magma fluctuates through these processes, the number density of phenocrysts develops through melting and crystallization (e.g., Simakin and Bindeman 2008). As the pre-existing crystals can grow during decompression or become a heterogeneous nucleation site, thereby controlling the evolution behavior of supersaturation in the melt, the change in the number density of phenocrysts in the reservoir seems to influence decompression-induced crystallization. The heating of magma in the reservoir also results in a homogeneous melt structure. The effect of melt homogeneity on decompression-induced crystallization is clarified by comparing two decompression experiments. Fig. 1 shows the number density of plagioclase microlites reported by Brugger and Hammer (2010) and Riker et al. (2015), where the values reported by Brugger and Hammer (2010) are markedly higher than those reported by Riker et al. (2015). In these two studies, the experimental conditions (decompression history, temperature, final pressure, and water-saturated conditions) and magma composition were similar. However, the starting materials were prepared using different procedures. The starting materials used by Brugger and Hammer (2010) were glassy materials from natural pumices, whereas those used by Riker et al. (2015) were synthesized by melting a mixture of oxides and carbonates at a temperature of 1450°C. This difference may explain the difference in number density as superheating above the liquidus temperature produces a homogeneous melt structure (fully relaxed melt) and suppresses nucleation, as demonstrated in the cooling experiments (Sato, 1995; Pupier et al., 2008; Shea and Hammer, 2013; Vetere et al., 2013; da Silva et al., 2017; First et al., 2020).

In this study, we investigated the effects of pre-existing crystals and melt homogeneity on crystallization during magma decompression. The starting materials were prepared with a rhyodacite composition via heating at different super-liquidus temperatures (940, 970, 1050, and 1300°C) and sub-liquidus temperature (900°C), followed by annealing at the same temperature (900°C) and pressure (130 MPa). Finally, the samples were subjected to the same decompression history and the obtained crystal textures were compared. Our experiments clearly indicate that pre-existing crystals enhance crystal growth and crystals are hard to nucleate in the homogenized melt, in line with the findings of the cooling experiments.

EXPERIMENTAL AND ANALYTICAL METHODS

Synthesis of the starting materials

We prepared four starting materials for the decompression experiments using rhyodacite pumice from the 1977 eruption of the Usu volcano, Japan (Katsui et al., 1978; Niida et al., 1980). The powdered pumices were heated at five temperatures (900, 940, 970, 1050, or 1300°C) in an internally heated pressure vessel (IHPV) or cold-seal pressure vessel (CSPV) and then annealed under magma reservoir conditions of 900°C and 130 MPa, which is slightly below the liquidus temperature of 920°C (Ohnishi and Tomiya, 2018). The pumices from the 1977 eruption of the Usu volcano include phenocrysts of plagioclase (1–6%; Oba and Katsui, 1983), orthopyroxene and Fe-Ti oxide, and plagioclase microlites in the groundmass.

We first washed rhyodacite pumice seven times with distilled water using an ultrasonic washer for 5 min. The washed pumice was dried overnight in an oven at a temperature of 110°C and then crushed and ground in a mortar for ~1 h. In the IHPV experiments at temperatures of 940, 970, 1050, and 1300°C, the same powder sample of approximately 195 mg was loaded into a platinum tube with a diameter of 5 mm, with 6 wt% water, and the tube was welded shut. Using the platinum tube for IHPV experiments, the iron content in samples decreased from 3.8 to 2.4 wt% (3.8 wt% for bulk rock composition from Matsumoto and Nakagawa, 2010) owing to the absorption loss from sample to the platinum tube; however, this decrease in the iron content does not cause significant difference (<10°C) in plagioclase liquidus, which is related to the definition of superheating, based on the MELTS calculation (Gualda et al., 2012; Ghiorso and Gualda, 2015). Repeated weighing and heating at 110°C were performed to check for water leakage from the capsule. In the CSPV experiment at 900°C, a 40 mg powder sample and 6 wt% water were loaded into a gold tube with a diameter of 5 mm. The tube was then welded shut. We rechecked for leakage by heating the capsule at 110°C and weighing the capsule. Water saturation was ensured under the following experimental conditions.

The IHPV experiments at 940, 970, 1050, and 1300°C were conducted using argon gas as the pressure medium at the Geological Survey of Japan (GSJ/AIST) (HARM–200 and SMC–5000; Tomiya and Miyagi, 2001; Tatsumi and Suzuki, 2009; Tomiya et al., 2010). The samples were heated at 940, 970, 1050, and 1300°C under 130 MPa pressure for 48, 48, 48, and 2 h, respectively. The temperature was then isobarically decreased to 900°C at a rate of 400°C/day, and the samples were annealed for 138, 137, 110, and 136 h, respectively (Fig. 2a, b). This condition, i.e., 900°C and 130 MPa, corresponds to the magma reservoir condition, under which plagioclase, orthopyroxene, and magnetite are stable (Ohnishi and Tomiya, 2018). Finally, the samples were quenched by dropping into a cooler zone (<200°C). The CSPV experiment was performed at Tohoku University using water as the pressure medium. In this experiment, the sample was heated at a temperature of 900°C and a pressure of 130 MPa for 72 h and then cooled rapidly by dropping into a water-cooled zone. The information for starting material syntheses is summarized in Table 1.

After the runs, we opened the capsules carefully, and the recovered samples were cut into ~1 mm cubes for decompression experiments. Small chips of the remaining samples were mounted using resin to analyze the chemical composition and crystal texture of the starting materials. Hereafter, we denote the synthesized starting materials without superheating (just annealed at 900°C) and already superheated at 940, 970, 1050, and 1300°C as 900st, 940st, 970st, 1050st, and 1300st, respectively.

Decompression experiments

Decompression experiments were conducted at Tohoku University using a CSPV with a syringe pump (Okumura et al., 2021). Using this system, we can precisely control decompression rates. For the decompression experiments, the synthesized samples (~1 mm cubes) were loaded into a gold tube (3 mm in diameter) with a small amount of water (0.1~0.3 mg) to achieve water saturation condition. The gold tubes were then welded shut, heated at 110°C, and weighed to check for water leakage.

In the decompression experiments using the CSPV, we first increased the furnace temperature to 900°C at 130 MPa, and then a filler rod was used to position the samples in the hotspot of the furnace. The sample was annealed at 900°C for 1 h and then isothermally and continuously decompressed to 30 MPa at rates of 5, 20, or 100 MPa h^{-1} (Fig. 2c, d). To validate the conditions before decompression, annealing experiments without decompression were performed at 900°C and 130 MPa for 1 h. An annealing experiment at 900°C and 30 MPa for 72 h was conducted to reveal the equilibrium texture at 900°C and 30MPa using 940st as a starting material. After the experiments, the capsules were embedded in resin, and the samples were investigated as described in the following sections. The information for all runs is summarized in Table 2.

Analytical methods

The chemical compositions of the glass in the groundmass and plagioclase were analyzed using energy-dispersive X-ray spectrometry (EDS, Oxford INCA) attached to a field-emission type scanning electron microscope (FE-SEM, JEOL JSM-7001F) at Tohoku University. The accelerating voltage and beam current were 15 kV and 1.4 nA (on a Co standard), respectively, and the counting time was 60 s. The glass composition was analyzed in scanning mode, and the plagioclase composition was analyzed in point mode. For large plagioclase crystals with a width of >10 μm, the core and rim compositions were analyzed, whereas the core and rim were not distinguished during the measurement of tiny crystals with a width of <10 μm. All the analytical results are listed in Table 3.

We obtained backscattered electron (BSE) images using field-emission type scanning electron microscopes (JEOL JSM-7001F and JEOL JSM-7100F at Tohoku University) with an acceleration voltage of 15 kV. For most quantitative measurements of the texture, images obtained at a magnification of 500× were used; however, samples containing large crystals were imaged at 250× magnification. The areal number density (N_A, the number of crystals per unit area) and areal fraction (ϕ) of plagioclase crystals on a vesicle-free basis were obtained using the image processing software package, ImageJ Fiji (Schindelin et al., 2012). The characteristic two-dimensional crystal size (S_N) is expressed as the square root of the mean crystal area, $S_N = (\phi / N_A)^{1/2}$. Quantitative data for each sample were obtained by analyzing three images.

For all starting materials, X-ray elemental mappings were obtained using the same SEM-EDS system. The accelerating voltage, beam current, and working distance were set to 15 kV, 5 nA, and 10 mm, respectively. Images were obtained with a magnification of 1500×. The image resolution and pixel size were 512 × 384 and 0.16 × 0.16 μm, respectively.

The water content of the 1300st was determined using an FT-IR microspectrometer (Nicolet iN-10, Thermo Fisher Scientific Inc.). A doubly polished thin section of the glass sample of 1300st was used. The typical size of the thin section was 1×1 mm, and its thickness was 156 μm. The aperture size of the IR measurements was set to 50×50 μm. The peak intensities of 5230 (H_2O) and 4500 (OH) cm^{-1} bands after background correction with two straight lines and the molar absorptivities of Ohlhorst et al. (2001), i.e., 1.41 and 1.19 L mol^{-1} cm^{-1} for the 5230 and 4500 cm^{-1} bands, respectively, were employed.

RESULTS

Starting materials for the decompression experiments

The BSE images of the starting materials are shown in Fig. 3. No crystals were observed in the 1300st sample, and only magnetite was found in the 1050st sample. In contrast, plagioclase, magnetite, and pyroxene were found in the 900st, 940st, and 970st samples. It should be noted that plagioclase, orthopyroxene and magnetite are stable under the annealing conditions of 900°C and 130 MPa (Ohnishi and Tomiya, 2018), and the annealing duration (72–138 h at 900°C) seems to be sufficient for the samples to reach equilibrium according to previous studies (Brugger and Hammer, 2010; Riker et al., 2015), although no crystals were observed in the 1300st sample and only magnetite was found in the 1050st sample.

Plagioclase, magnetite, and pyroxene in the 900st sample show euhedral and irregular rims; sometimes, the irregular rims are curvilinear. No clear compositional zoning is found in these crystals. In contrast, the crystals in the 940st and 970st samples appear blocky. The plagioclase in the 940st sample shows clear compositional zoning (Fig. 3d), and those in the 970st sample seem to have zoning. These results suggest that almost all crystals in the 900st sample are relicts. Most of the crystals in the 940st and 970st samples also resulted from the growth of relicts. The 900st sample seems to contain more crystals than the 940st and 970st samples (the number density is reported in the following section). The number density of plagioclase crystals is markedly higher than those of pyroxene and magnetite; hence, we focus only on plagioclase crystals in the following sections. The total water content of the 1300st sample obtained by FT-IR spectroscopy was ~4.5 wt%, which is fairly consistent with the water content saturated under experimental conditions, i.e., 4.4 wt% based on the model of Newman and Lowenstern (2002). We could not measure water contents in other samples including small crystals, but we expect that all samples were saturated with water because we used the same sample/water ratio and experimental conditions.

Qualitative description of the run products

We first compared the run products annealed at 900°C for 1 h just before the decompression (Fig. 4). However, no qualitative variations are observed in the run products of the annealing experiment and starting materials. This observation indicates that annealing for 1 h before decompression did not cause remarkable variation in the crystal texture and the number density and that crystallinity of the run products without decompression were almost the same as those of the starting materials within the errors (Tables 1 and 2).

In Fig. 5, we show BSE images of the run products after decompression. In the run products of the 1050st and 1300st samples, no plagioclase was found when the decompression rate was 100 MPa h^{-1}, whereas plagioclases with a length of ~100 μm and width of <10 μm were formed at decompression rates of 5 and 20 MPa h^{-1}. However, these plagioclase crystals seem to be heterogeneously formed along the capsule walls or bubbles (Fig. 6). The morphology of crystals obtained at 5 MPa h^{-1} is hopper and swallowtail, and that obtained at 20 MPa h^{-1} is skeletal. According to Shea and Hammer (2013), the morphology changes from hopper and swallowtail to skeletal with increasing undercooling. Because a high decompression rate is expected to result in large undercooling, the evolution of plagioclase morphology is consistent with the expected behavior.

For runs with the 970st sample, no large qualitative differences appeared between the run products with and without decompression (Figs. 4c and 5c). Only a thin overgrowth of plagioclase with a sodic composition was observed at 5 and 20 MPa h^{-1}.

In the run products of the 940st samples obtained at a decompression rate of 100 MPa h^{-1} (Fig. 5d), plagioclases with lengths of a few micrometers are found in the melt, which are markedly smaller than pre-existing crystals (~30 μm). Larger plagioclases, i.e., several micrometers to ~20 μm, are observed after decompression at 5 and 20 MPa h^{-1}. These crystals are thought to nucleate and grow during decompression. In addition to these tiny plagioclases, overgrowth rims are observed on plagioclase with a length of >~30 μm at 5 and 20 MPa h^{-1}.

In the run products of the 900st sample obtained at 20 MPa h^{-1} (Fig. 5e), the number density is high, as described in the following section. After decompression at 5 MPa h^{-1}, plagioclase appears to be slightly larger.

The length of tiny plagioclase shows large variation depending on starting materials; hence, we consider tiny plagioclase with a width of <10 μm as crystals formed during decompression.

Quantitative description of plagioclase: number density, size, and crystallinity

We indicate N_A, S_N, and ϕ of plagioclase in the run products without and with decompression in Figs. 7 and 8, respectively. To clarify the change in ϕ and N_A during decompression, the crystallinity and number density obtained by subtracting ϕ and N_A without decompression from those after decompression are also shown in Fig. 9. In the run products without decompression, N_A decreased with increasing heating temperature from 900 to 1300°C (Fig. 7a) and S_N increased with heating temperature. We could not define S_N for the samples heated at 1050 and 1300°C because both N_A and ϕ were almost zero (Fig. 7b). These results indicate that the degree of dissolution of pre-existing plagioclase in the pumice depended on the heating temperature, i.e., 900, 940, 970, 1050, or 1300°C, and then crystallization during annealing at 900°C was controlled by growth rather than nucleation. This is because the degree of supercooling is small, that is, the difference between liquidus and experimental temperatures is 20°C, at which the growth controls the crystallization (e.g., Couch et al., 2003b; Jiusti et al., 2020). These findings are supported by the observation of relicts and compositional zoning in the 940st and 970st samples, but no clear zoning in the 900st sample. In addition, the crystals in the 940st and 970st samples are mainly euhedral and blocky.

In the run products with decompression, N_A is higher for the samples decompressed at 20 MPa h^{-1} than for those decompressed at 5 and 100 MPa h^{-1} for the runs with the 900st and 940st samples (Figs. 8a and 9a). In the 970st sample, no clear variation in N_A is found. S_N varied only slightly from that in the run products without decompression (Fig. 8b), although ϕ increased after decompression (Figs. 8c and 9b). This finding indicates that the newly nucleated crystals were similar in size to the pre-existing crystals or that crystals of different sizes, i.e., small newly formed crystals and large crystals that grew during decompression, were both present owing to the combined effect of nucleation and growth. Figs. 4 and 5 clearly show the coexistence of small newly formed crystals and large pre-existing crystals; hence, no clear variation in S_N is observed in the run products of the 970st sample because of the combined effect of nucleation and growth. In the 1050st and 1300st samples, N_A decreases as the decompression rate increases from 5 to 100 MPa h^{-1}.

The value of ϕ decreases as the decompression rate increases from 5 to 100 MPa h^{-1} for all samples. The equilibrium crystallinity at 900°C and 30 MPa was ~41 area% based on the results of the annealing experiments for 72 h (ϕ_{EQ}) (Table 2). This result indicates that crystallization did not reach equilibrium, even in the runs at 5 MPa h^{-1}.

Our results indicate that the crystal texture was strongly influenced by the highest heating temperature during the synthesis of the starting materials. At higher temperatures (970, 1050, and 1300°C), the number density of plagioclase was low in both the starting materials and run products after decompression. Only small increases were found for the runs with the 970st sample, and almost no crystallization was found after the run with the 1050st and 1300st samples at 100 MPa h^{-1}. In contrast, the number densities of plagioclase in the 900st and 940st samples were higher than those in the 970st, 1050st, and 1300st samples, and the increase in the number density after decompression was also large in the 900st and 940st samples. Namely, the nucleation rate was high in the samples that initially had a high number density. These results are inconsistent with the expectation from crystallization kinetics that the degree of supersaturation is decreased by the growth of pre-existing crystals and that nucleation does not become dominant if the decrease with growth occurs rapidly enough (e.g., Shea and Hammer, 2013). Rather, these results indicate a difference in the homogeneity of the melt structure controls crystal texture. When the sample was heated at a higher temperature, the crystals dissolved and the melt structure relaxed, resulting in a homogeneous structure. We will discuss this in the following section.

Chemical composition: glass and plagioclase.

The chemical compositions of glass part and plagioclase are summarized in Table 3 and the K_2O content in the glass is shown in Fig. 10. The K_2O content decreases with an increase in the decompression rate. This result indicates that the degree of non-equilibrium is larger, that is, the crystallinity is lower at higher decompression rates as K_2O is an incompatible element. Additionally, the K_2O content is low when the heating temperature was high.

Fig. 11 indicates the An contents obtained from the rim of plagioclase and tiny plagioclase (<~10 μm). It should be noted that the core includes both pre-existing crystals and newly formed crystals, which cannot be distinguished using chemical composition; thus, we investigated only the rim and tiny crystals and did not consider the data from the cores in this study. The rim compositions of the 940st and 970st samples and the annealed samples with 900st, 940st, and 970st samples show a peak around An_{60}–An_{65}. This An content is almost consistent with the chemical composition of the rim of plagioclase phenocrysts from the 1977 eruption of Usu volcano (Tomiya and Takahashi, 2005), indicating that the phenocrysts may be in equilibrium at 900°C and 130 MPa. The An content of the rims of the 900st sample shows the broad range because plagioclase in the sample consists of relicts of plagioclase phenocrysts and microlites, as discussed above. No plagioclase was found in the 1050st and 1300st samples, and hence no rim data were obtained for the runs with the 1050st and 1300st samples.

The average An content of the rims of the run products with the 900st and 940st samples after decompression clearly decreases with decreasing decompression rate. However, the average An content at 20 MPa h^{-1} is the lowest in the runs with the 970st sample. In contrast, the lowest An content indicates complex behavior as follows. For the runs with the 940st and 970st samples, the An content at 20 MPa h^{-1} is the lowest, while the lowest An content decreases gradually with decreasing decompression rate from 100 to 5 MPa h^{-1} in the runs with the 900st sample.

Tiny plagioclases were found in all run products, except runs with the 1050st and 1300st samples at 100 MPa h^{-1}. In the runs with the 1050st and 1300st samples at 5 and 20 MPa h^{-1}, the An content distributions are narrow, and the average values are low compared with those of runs with other starting materials. The An contents of the run products of the 970st sample at 100 MPa h^{-1} are slightly lower than those at 5 and 20 MPa h^{-1}. In contrast, the An content clearly decreases with decreasing decompression rate when the 940st sample was used as the starting material. The An content of the run products of the 900st sample shows no clear variation.

DISCUSSION

Effects of pre-existing crystals and melt homogeneity on decompression-induced crystallization

Our experiments indicated that the pre-existing crystals and melt homogeneity affect the crystal number density and total crystallinity after decompression. In runs with the 970st, 940st, and 900st samples, it is clearly found that pre-existing crystals control the number density of crystals (Fig. 9a). The number density of plagioclase formed during decompression was higher when the highest heating temperature was lower (Fig. 9). The number density of plagioclase formed during decompression increased with a decrease in the highest heating temperature from 970 to 900°C. These results indicate that nucleation from the melt occurred easily when the initial number density was high. This result contradicts the common-sense idea that nucleation occurs when the supersaturation is sufficiently high to overcome the energy barrier for homogenous nucleation, and that the growth of pre-existing crystals or heterogeneous crystallization from them decreases supersaturation (e.g., Andrews and Befus, 2020). Mollo et al. (2012) reported that plagioclase may nucleate on pre-existing crystals; however, our results are inconsistent with this idea, because no clear heterogeneous nucleation is observed (Fig. 5). The results of our experiments can be explained by considering that higher heating temperatures result in a more homogeneous melt structure. In the runs with the 970st sample, the melt structure was relatively homogeneous; thus, nucleation was suppressed, and the growth of pre-existing crystals was dominant. In the runs with the 940st sample, the number density was higher than that in the runs with the 970st sample. Because the temperature of 940°C is above the liquidus temperature, the crystals dissolved during heating, despite the survival of large crystals, resulting in relicts. Therefore, our results can be explained by considering that the melt structure did not relax perfectly from a crystal-like structure (pre-crystal clusters) to a homogeneous melt structure during heating at 940°C, and that the pre-crystal clusters contributed to nucleation during decompression.

The pre-crystal clusters were difficult to identify in this study. Fig. 12 shows composition maps of the starting materials, which indicate no clear signatures in the glass parts. In contrast, relicts with a few micrometers in size are clearly found in the 900st and 940st samples (Figs. 12d and 12e). Additionally, no crystals in the glass parts were observed in the BSE images even at high magnification (20,000×, Fig. 13), indicating that the pre-crystal clusters were not crystal relicts. If the homogenization of a melt is controlled by element diffusion, we may be able to estimate the timescale of homogenization based on diffusion timescale (Vetere et al., 2013). Here, we assume Si diffusion at superheating conditions; the diffusion coefficients are 2.3×10^{-2} and 1.3×10^{-2} μm^2 s^{-1} at 970 and 940°C, respectively, based on Eyring relationship (Chakraborty, 1995). The distance between crystals is approximately 50 μm; hence, the estimated diffusion timescales are 1.1×10^5 and 1.9×10^5 s for 970 and 940°C, respectively, based on the relationship of (l^2/D), where l and D represent the distance between crystals and diffusion coefficient, respectively. These timescales are roughly the same as the heating time; hence, we infer that the crystals dissolved during superheating, but the melt structure was not perfectly homogenized through diffusion.

Melt homogeneity strongly controls crystal nucleation, and hence, the number density of the crystals. In the runs with the 1300st and 1050st samples, almost no crystals were observed in the run products at a decompression rate of 100 MPa h^{-1}. The low crystallinity and plagioclase morphology in the run products at 5 and 20 MPa h^{-1} also indicate that crystallization occurred only when high supersaturation was achieved. These observations differed from those obtained in runs using the starting materials heated at lower temperatures (970st and 940st, and 900st). These results clearly indicate that melt homogenization by heating influences the crystal texture formed by magma ascent and decompression.

The quantitative description of the effect of heating on melt homogenization remains unclear. In our experiments, the 50°C superheating for 48 h (970st) resulted in melt homogenization, whereas the melt was not homogenized and the pre-crystal clusters existed in samples with the 20°C superheating for 48 h (940st).

In summary, nucleation and growth are controlled by heating and cooling before decompression through the degree of crystal dissolution and melt relaxation. It should be noted that the pre-crystal clusters originated from the experimental procedure used herein; however, they may also be formed in the natural system by increasing and decreasing magma temperature.

Comparison with previous studies

We compared our data with those obtained under similar experimental conditions in previous studies (Brugger and Hammer, 2010; Riker et al., 2015) (Fig. 14). Based on our experiments, the number density of microlites formed during decompression was high in the sample without superheating (900st). The number densities observed in the experiments without superheating by Brugger and Hammer (2010) were markedly higher than those in the superheated samples in this study and Riker et al. (2015), as observed at low decompression rates (Fig. 14). As discussed in the previous section, nucleation is suppressed in samples homogenized by superheating, resulting in the occurrence of high supersaturation, which could cause high nucleation rate. However, a comparison of the number density in the samples with and without superheating indicates that the number density is high in the samples without superheating. This finding implies that the high number density in samples without superheating originates from heterogeneous nucleation resulting from the presence of pre-crystal clusters in natural samples.

In natural samples, high number densities ($>\sim 10^4$ mm^{-2}) are often observed, and their origin is an unsolved problem (e.g., Martel, 2012; Riker et al., 2015). When natural samples without superheating were used as the starting materials in the decompression experiments, these high number densities were reproduced (Brugger and Hammer, 2010; Befus and Andrews, 2018). In contrast, the maximum number densities observed in experiments with superheating were 10^4 mm^{-2} (Riker et al., 2015; this study), which is lower than the high values observed in some natural samples. To explain these high number densities, Riker et al. (2015) proposed that the fluxing of a CO_2-rich fluid into initially H_2O-rich magma lowers the partial pressure of water and enhances rapid crystallization in nature. Additionally, magma decompression during ascent may result in cooling because of adiabatic gas expansion (Mastin and Ghiorso, 2001). In addition to the contribution of heterogeneous nucleation associated with pre-crystal clusters, these unrecognized mechanisms may contribute to the high number densities observed in natural samples. Recently, Lindoo and Cashman (2021) performed decompression experiments to simulate Vulcanian eruptions. In particular, they reproduced pressure fluctuations during intermittent explosions and reported that rapid deformation in magma may result in an increase in the crystal number density through the extensive disruption of crystals.

IMPLICATIONS

We experimentally demonstrated that the crystal texture formed during magma decompression depends on the degree of superheating before decompression. This finding indicates that the degree of homogeneity of the melt structure is an important factor in controlling crystallization kinetics. In actual eruptions, the magma temperature before the eruption fluctuates because of cooling in the cold crust and heating due to interactions with the hotter magmas in the reservoir (e.g., Cooper and Kent, 2014; Tomiya et al., 2013). As the temperature fluctuates, the chemistry and morphology of the phenocrysts develop through elemental diffusion, crystallization, and melting. In many cases, silicic magmas undergo heating just before an eruption (e.g., Nakamura, 1995; Tomiya et al., 2013), which may result in a homogeneous melt structure and the occurrence of heterogeneity through crystal dissolution, and finally affect the crystal texture in the magma that erupts to the surface. Based on our experiments, the 50°C superheating for 48 h is sufficient to produce a homogeneous melt structure and suppress decompression-induced nucleation. On the other hand, the inefficient superheating observed in this study (superheating by 20°C for 48 h) may result in the formation of pre-crystal clusters; this heterogeneity may also enhance bubble formation through heterogeneous nucleation (Shea, 2017; Hajimirza et al., 2021) and hence control the explosivity of the eruption. To understand these processes, we need to clarify the relationship between crystal formation and the nanoscale melt structure in future studies.

Acknowledgments.

We would like to thank Masashi Ushioda and Takayuki Nakatani for their support during the IHPV experiments. Part of this work was conducted within the AIST Research Assistant Program for K. M. This study was supported by the Grand-in-aid for Scientific Research in Japan (Nos. 18H01296, 22H00161) to S.O., by the International Joint Graduate Program in Earth and Environmental Sciences, Tohoku University(GP-EES), and by JST SPRING, Grant Number JPMJSP2114 to K. M. The authors thank Gianluca Iezzi and anonymous reviewers for critical review and the Editor Don R. Baker.

References.

Andrews, B.J., and Befus, K.S. (2020) Supersaturation nucleation and growth of plagioclase: a numerical model of decompression-induced crystallization. Contributions to Mineralogy and Petrology, 175, 23.

Befus, K.S., and Andrews, B.J. (2018) Crystal nucleation and growth produced by continuous decompression of Pinatubo magma. Contributions to Mineralogy and Petrology, 173, 92.

Brugger, C.R., and Hammer, J.E. (2010) Crystallization kinetics in continuous decompression experiments: Implications for interpreting natural magma ascent processes. Journal of Petrology, 51, 9, 1941–1965.

Cashman, K.V. (1992) Groundmass crystallization of Mount St. Helens dacite, 1980–1986: A tool for interpreting shallow magmatic processes. Contributions to Mineralogy and Petrology, 109, 431–449.

Chakraborty, S. (1995) Diffusion in silicate melts. In: Stebbins, J.F., Dingwell, D.B., McMillan, P.W. (Eds.), Structure and dynamics of Silicate Melts: Reviews in Mineralogy and Geochemistry, 32, pp. 411–497.

Cichy, S.B., Botcharnikov, R.E., Holtz, F., and Behrens, H. (2011) Vesiculation and microlite crystallization induced by decompression: a case study of the 1991–1995 Mt. Unzen eruption (Japan). Journal of Petrology, 52, 7–8, 1469–1492.

Cooper, K.M., and Kent, A.J.R. (2014) Rapid remobilization of magmatic crystals kept in cold storage. Nature, 506, 480–483.

Couch, S., Harford, C.L., Sparks, R.S.J., and Carroll, M.R. (2003a) Experimental constraints on the conditions of formation of highly calcic plagioclase microlites at the Soufrière Hills Volcano, Montserrat. Journal of Petrology, 44, 8, 1455–1475.

Couch, S., Sparks, R.S.J., and Carroll, M.R. (2003b) The kinetics of degassing-induced crystallization at Soufrière Hills Volcano, Montserrat. Journal of Petrology, 44, 8, 1477–1502.

da Silva, M.M., Holtz, F., and Namur, O. (2017) Crystallization experiments in rhyolitic systems: The effect of temperature cycling and starting material on crystal size distribution. American Mineralogist, 102, 2284–2294.

Fiege, A., Vetere, F., Iezzi, G., Simon, A., and Holtz, F. (2015) The roles of decompression rate and volatiles (H_2O + Cl $\pm$ CO_2 $\pm$ S) on crystallization in (trachy-)basaltic magma. Chemical Geology, 411, 310–322.

First, E.C., Leonhardi, T.C., and Hammer, J.E. (2020) Effects of superheating magnitude on olivine growth. Contributions to Mineralogy and Petrology, 175:13.

Ghiorso M.S., and Gualda, G.A.R. (2015) An H_2O–CO_2 mixed fluid saturation model compatible with rhyolite-MELTS. Contributions to Mineralogy and Petrology, 169, 53.

Gonnermann, H.M., and Manga, M. (2003) Explosive volcanism may not be an inevitable consequence of magma fragmentation. Nature, 426, 432–435.

Gualda, G.A.R., Ghiorso, M.S., Lemons, R.V., and Carley T.L. (2012) Rhyolite-MELTS: A modified calibration of MELTS optimized for silica-rich, fluid-bearing magmatic systems. Journal of Petrology, 53, 875–890.

Hajimirza, S., Gonnermann, H.M., and Gardner, J.E. (2021) Reconciling bubble nucleation in explosive eruptions with geospeedometers. Nature Communications, 12, 283.

Hammer, J.E., and Rutherford, M.J. (2002) An experimental study of the kinetics of decompression-induced crystallization in silicic melt. Journal of Geophysical Research: Solid Earth, 107, B1, ECV 8–1–ESV 8–24.

Jiusti, J., Zanotto, E.D., Cassar, D.R., and Andreeta, M.R.B. (2020) Viscosity and liquidus-based predictor of glass-forming ability of oxide glasses. Journal of the American Ceramic Society, 103, 921–932.

Katsui, Y., Oba, Y., Onuma, K., Suzuki, T., Kondo, Y., Watanabe, T., Niida, K., Uda, T., Hagiwara, S., Nagao, T., Nishikawa, J., Yamamoto, M., Ikeda, Y., Katagawa, H., Tsuchiya, N., Shirahase, M., Nemoto, S., Yokoyama, S., Soya, T., Fujita, T., Inaba, K., and Koide, K. (1978) Preliminary report of the 1977 eruption of Usu volcano. Journal of the Faculty of Science, Hokkaido University. Series IV, 18(3), 385–408.

Kent, A.J.R, Darr, C., Koleszar, A.M., Salisbury, M.J., and Cooper, K.M. (2010) Preferential eruption of andesitic magmas through recharge filtering. Nature Geoscience, 3, 631–636.

Lindoo, A., and Cashman, K.V. (2021) High crystal number densities from mechanical damage. Frontiers in Earth Science, 9:659459. doi: 10.3389/feart.2021.659459

Martel, C. (2012) Eruption dynamics inferred from microlite crystallization experiments: Application to plinian and dome-forming eruptions of Mt. Pelée (Martinique, Lesser Antilles). Journal of Petrology, 53, 4, 699–725.

Martel, C., and Schmidt, B.C. (2003) Decompression experiments as an insight into ascent rates of silicic magmas. Contributions to Mineralogy and Petrology, 144, 4, 397–415.

Mastin, L.G., and Ghiorso, M.S. (2001) Adiabatic temperature changes of magma-gas mixtures during ascent and eruption. Contributions to Mineralogy and Petrology, 141, 307–321.

Matsumoto, A., and Nakagawa, M. (2010) Formation and evolution of silicic magma plumbing system: Petrology of the volcanic rocks of Usu volcano, Hokkaido, Japan. Journal of Volcanology and Geothermal Research, 196, 185–207.

Melnik, O., and Sparks, R.S.J. (1999) Nonlinear dynamics of lava dome extrusion. Nature, 402, 37–41.

Mollard, E., Martel, C., and Bourdier, J. (2012) Decompression-induced crystallization in hydrated silica-rich melts: Empirical models of experimental plagioclase nucleation and growth kinetics. Journal of Petrology, 53, 8, 1743–1766.

Mollo, S., Iezzi, G., Ventura, G., Cavallo, A., and Scarlato, P. (2012) Heterogeneous nucleation mechanisms and formation of metastable phase assemblages induced by different crystalline seeds in a rapidly cooled andesitic melt. Journal of Non-Crystalline Solids, 358, 1624–1628.

Nakamura, M. (1995) Continuous mixing of crystal mush and replenished magma in the ongoing Unzen eruption. Geology, 23(9), 807–810.

Newman, S., and Lowenstern, J.L. (2002) VOLATILECALC: a silicate melt–H_2O–CO_2 solution model written in Visual Basic for excel. Computers & Geosciences, 28, 5, 597–604.

Niida, K., Katsui, Y., Suzuki, T., and Kondo, Y. (1980) The 1977-1978 eruption of Usu volcano. Journal of the Faculty of Science, Hokkaido University. Series 4, 19(3), 357–394.

Oba, Y., and Katsui, Y. (1983) Petrology of the felsic volcanic rocks from Usu volcano, Hokkaido, Japan. Journal of Mineralogy, Petrology and Economic Geology, 78, 123–131.

Ohlhorst, S., Behrens, H., and Holts, F. (2001) Compositional dependence of molar absorptivities of near-infrares OH- and H_2O bands in rhyolitic to basaltic glasses. Chemical Geology, 174, 5–20.

Ohnishi, S., and Tomiya, A. (2018) Pre-eruptive processes of the 2000 eruption of Usu volcano, Japan. Program and Abstracts, Volcanological Society of Japan, 2018, 146 (in Japanese).

Okumura, S., Ishibashi, H., Itoh, S., Suzumura, A., Furukawa, Y., Miwa, T., and Kagi, H. (2021) Decompression experiments for sulfur-bearing hydrous rhyolite magma: Redox evolution during magma decompression. American Mineralogist, 106, 216–225.

Pupier, E., Duchene, S., and Toplis, M.J. (2008) Experimental quantification of plagioclase crystal size distribution during cooling of basaltic liquid. Contributions to Mineralogy and Petrology, 155, 555–570.

Riker, J.M., Cashman, K.V., Rust, A.C., and Blundy, J.D. (2015) Experimental constraints on plagioclase crystallization during H_2O- and H_2O–CO_2-saturated magma decompression. Journal of Petrology, 56, 10, 1967–1998.

Sato, H. (1995) Textural difference between pahoehoe and aa lavas of Izu-Oshima volcano, Japan – an experimental study on population density of plagioclase. Journal of Volcanology and Geothermal Research, 66, 101–113.

Schindelin, J., Arganda-Carreras, I., Frise, E., Kaynig, V., Longair, M., Pietzsch, T., Preibisch, S., Rueden, C., Saalfeld, S., Schmid, B., Tinevez, J., White, D.J., Hartenstein, V., Eliceiri, K., Tomancak, P., and Cardona, A. (2012) Fiji: an open-source platform for biological-image analysis. Nature Methods, 9, 676–682.

Shea, T. (2017) Bubble nucleation in magmas: A dominantly heterogeneous process? Journal of Volcanology and Geothermal Research, 343, 155–170.

Shea, T., and Hammer, J.E. (2013) Kinetics of cooling- and decompression-induced crystallization in hydrous mafic-intermediate magmas. Journal of Volcanology and Geothermal Research, 260, 127–145.

Simakin, A.G., and Bindeman, I.N. (2008) Evolution of crystal sizes in the series of dissolution and precipitation events in open magma systems. Journal of Volcanology and Geochemical Research, 177, 4, 997–1010.

Tatsumi, Y., and Suzuki, T. (2009) Tholeiitic vs calc-alkalic differentiation and evolution of ark crust: constraints from melting experiments on a basalt from the Izu–Bonin–Mariana arc. Journal of Petrology, 50, 8, 1575–1603.

Tomiya, A., and Miyagi, I. (2001) An internally heated gas-medium high-pressure apparatus with quenching device and decompression speed controller. Program and Abstracts, Volcanological Society of Japan 2001(2), 177 (in Japanese).

Tomiya, A., and Takahashi, E. (2005) Evolution of the magma chamber beneath Usu volcano since 1663: a natural laboratory for observing changing phenocryst compositions and textures. Journal of Petrology, 46, 12, 2395–2426.

Tomiya, A., Takahashi, E., Furukawa, N., and Suzuki, T. (2010) Depth and evolution of a silicic magma chamber: Melting experiments on a low-K rhyolite from Usu volcano, Japan. Journal of Petrology, 51, 6, 1333–1354.

Tomiya, A., Miyagi, I., Saito, G., and Geshi, N. (2013) Short time scales of magma-mixing processes prior to the 2011 eruption of Shinmoedake volcano, Kirishima volcanic group, Japan. Bulletin of Volcanology, 75, 750.

Toramaru, A., Noguchi, S., Oyoshihara, S., and Tsune, A. (2008) MND (microlite number density) water exsolution rate meter. Journal of Volcanology and Geothermal Research, 175, 156–167.

Vetere, F., Iezzi, G., Behrens, H. Cavallo, A., Misiti, V., Dietrich, M., Knipping, J., Ventura, G., and Mollo, S. (2013) Intrinsic solidification behavior of basaltic to rhyolitic melts: A cooling rate experimental study. Chemical Geology, 354, 233–242.

Figure captions

Figure 1. Number density (N_A) of plagioclase microlite in run products of the decompression experiments reported by Brugger and Hammer (2010) (B&H 2010) and Riker et al. (2015) (Riker 2015).

Figure 2. (a) Temperature (T)–time (t) path of starting material synthesis, (b) Pressure (P)–time (t) path of starting material synthesis, (c) T–t path of decompression experiments, and (d) P–t path of decompression experiments.

Figure 3. Backscattered electron (BSE) images of the synthesized glasses (starting materials) superheated at (a) 1300°C, (b) 1050°C, (c) 970°C, and (d) 940°C using an internally heated pressure vessel and annealed at (e) 900°C using a cold seal pressure vessel. Plagioclase crystals (light grey; PL) and Fe-Ti oxide (light; OX) are found in (b)–(e).

Figure 4. Backscattered electron (BSE) images of the samples of (a) 1300st, (b) 1050st, (c) 970st, (d) 940st, and (e) 900st after annealing at 900°C for 1 h (e.g., run# 1300st1h). No clear change in crystal texture is observed compared with the

starting materials (BSE images) in Fig. 3.

Figure 5. Backscattered electron (BSE) images of the run products of (a) 1300st, (b) 1050st, (c) 970st, (d) 940st, and (e) 900st after decompression at 100, 20, and 5 MPa h^{-1} (e.g., run# 1300stdec100). Light grey particles represent plagioclase crystals.

Figure 6. Backscattered electron (BSE) images of the run products of (a) 1300st and (b) 1050st after decompression at 5 MPa^{-1} and 20MPa^{-1} near capsule wall. Crystals are heterogeneously formed along the capsule wall.

Figure 7. (a) Number density (N_A), (b) characteristic two-dimensional crystal size (S_N), and (c) areal fraction (ϕ) of plagioclase crystals in the run products without decompression vs. superheated temperature. In the sample superheated at 1300°C, no crystals are found. The error bars represent the standard deviation based on analyses of three images.

Figure 8. (a) Number density (N_A), (b) characteristic two-dimensional crystal size (S_N), and (c) areal fraction (ϕ) of plagioclase crystals in the run products after decompression vs. decompression rate. In the run with 1300stv2, no crystals are found at 100 MPa h^{-1}. The error bars represent the standard deviation based on analyses of three images.

Figure 9. (a) Number density of plagioclase crystal formed during decompression (N_A–$N_{A,\mathrm{anneal}}$) and (b) areal fraction of plagioclase crystals formed or grew during decompression (ϕ–ϕ_{anneal}) vs. decompression rate. The number density and areal fraction are calculated by the difference between those of the decompression (N_A, ϕ) and those of the annealing experiments ($N_{A,\mathrm{anneal}}$, ϕ_{anneal}).

Figure 10. K_2O content in glass parts of the run products vs. decompression rate. The error bars represent the standard deviation (see also Table 3).

Figure 11. Anorthite contents of plagioclase rim (grey box) and tiny plagioclase (open box) in the starting material, run product after annealing for 1 h (1 h annealing), and run products after decompression at 100, 20, and 5 MPa h^{-1}. The edges of each box and bar represent upper and lower quartile and the range of the anorthite content, respectively. The horizontal line inside each box represents median. The data are derived from experiments with (a) 1300st, (b) 1050st, (c) 970st, (d) 940st, and (e) 900st.

Figure 12. Composition map (Na, Al, and Ca) of the starting materials (a) 1300st, (b) 1050st, (c) 970st, (d) 940st, and (e) 900st with BSE images. In the BSE images, light grey and white particles represent plagioclase (PL) and Fe-Ti Oxide (OX), respectively.

Figure 13. Backscattered electron (BSE) images of the starting materials, (a)(b) 940st and (c)(d) 970st. No crystals were found in the BSE images even with high magnification (20,000×).

Figure 14. Number density (N_A) of plagioclase microlites in silicic magmas formed during decompression as a function of decompression rate. At low decompression rate, the N_A values obtained in runs with natural samples (B&H 2010, Brugger and Hammer, 2010) are markedly higher than those with superheated samples in this study (1300st, 1050st, 970st, 940st, and 900st) and the synthesized samples of Riker et al. (2015) (Riker 2015). P_f represents the final pressure after

decompression.

TABLE 1. Summary of starting material syntheses

Starting material#	T_s[a] and T_a[a] (°C)	t_s[b] (h)	t_{a1}[b] (h)	N_A[c] (mm^{-2})	ϕ[d]	S_N[e] (mm)
1300st	1300	2	136	0	0	0
1050st	1050	48	110	0	0	0
970st	970	48	137	363(186)[f]	0.102(0.061)	0.017(0.008)
940st	940	48	138	744(205)	0.047(0.021)	0.008(0.003)
900st	900	0	72	3247(240)	0.137(0.053)	0.006(0.002)

[a] "T_s" and "T_a" represent superheating and annealing temperatures, respectively, as indicated in Figure 2.

[b] "t_s" and "t_{a1}" represent the durations heated at superheating and annealing temperature, respectively.

[c] Number density of plagioclase crystals in starting materials.

[d] Areal fraction of plagioclase crystals.

[e] Characteristic two-dimensional crystal size of plagioclase crystals.

[f] The values in parentheses represent the standard deviation for analyses of three images (1σ).

TABLE 2. Run information

Run#	Type	t_{a2}[a] (h)	Rate ($MPah^{-1}$)	Final P (MPa)	N_A[b] (mm^{-2})	ϕ[c]	S_N[d] (mm)
1300st1h	Annealing	1	-	130	0	0	0
1300stdec100	Decompression	1	100	30	0	0	0
1300stdec20	Decompression	1	20	30	639(241)[e]	0.038(0.038)	0.008(0.006)
1300stdec5	Decompression	1	5	30	1522(610)	0.248(0.060)	0.013(0.003)
1050st1h	Annealing	1	-	130	16(24)	0.002(0.003)	0.010(0.013)
1050stdec100	Decompression	1	100	30	56(40)	0.003(0.004)	0.007(0.007)
1050stdec20	Decompression	1	20	30	167(130)	0.013(0.008)	0.009(0.008)
1050stdec5	Decompression	1	5	30	1265(475)	0.184(0.033)	0.012(0.003)
970st1h	Annealing	1	-	130	440(140)	0.097(0.007)	0.015(0.002)
970stdec100	Decompression	1	100	30	818(146)	0.177(0.071)	0.015(0.004)
970stdec20	Decompression	1	20	30	626(317)	0.136(0.051)	0.015(0.005)
970stdec5	Decompression	1	5	30	917(195)	0.241(0.043)	0.016(0.003)
940st1h	Annealing	1	-	130	739(226)	0.060(0.006)	0.009(0.002)
940stdec100	Decompression	1	100	30	2822(646)	0.141(0.031)	0.007(0.001)
940stdec20	Decompression	1	20	30	3834(350)	0.154(0.032)	0.006(0.001)
940stdec5	Decompression	1	5	30	2423(632)	0.263(0.044)	0.010(0.002)
Eq[f]	Equilibrium	1	100	30	12347(2255)	0.412(0.055)	0.006(0.001)
900st1h	Annealing	1	-	130	3342(446)	0.074(0.014)	0.005(0.001)
900stdec100	Decompression	1	100	30	7044(1286)	0.176(0.002)	0.005(0.000)
900stdec20	Decompression	1	20	30	7984(467)	0.214(0.008)	0.005(0.000)
900stdec5	Decompression	1	5	30	5340(416)	0.218(0.018)	0.006(0.000)

[a] "t_{a2}" represent the durations heated at 900°C under 130 MPa.

[b] Number density of plagioclase crystals.

[c] areal fraction of plagioclase crystals.

[d] characteristic two-dimensional crystal size of plagioclase crystals.

[e] The values in parentheses represent the standard deviation for analyses of three images (1σ).

[f] An "Eq" experiment was performed to check equilibrium crystallinity at 30 MPa. After decompression at 100 MPa/h, the sample was held at 30 MPa for 72 h.

TABLE 3. Chemical composition of matrix glass and plagioclase

Sample	SiO_2	TiO_2	Al_2O_3	FeO	MnO	MgO	CaO	Na_2O	K_2O	P_2O_5	*n* [a]	An_{rim} [b]	*n* [a]	An_{tiny} [b]	*n* [a]
1300st	71.76	0.49	15.30	1.94	0.14	0.96	4.04	4.21	1.10	0.07	7	-	-	-	-
1300st1h	71.88	0.55	14.97	2.03	0.28	0.99	4.04	4.08	1.13	0.04	6	-	-	-	-
1300stdec100	71.54	0.50	15.13	2.16	0.24	0.97	4.09	4.23	1.13	0.03	6	-	-	-	-
1300stdec20	71.43	0.49	15.11	2.61	0.19	0.96	3.75	4.16	1.25	0.07	6	-	-	48–56	11
1300stdec5	75.17	0.53	12.81	2.87	0.17	0.58	2.16	4.11	1.47	0.13	7	-	-	49–55	20
1050st	71.89	0.42	15.07	2.16	0.19	0.91	3.93	4.19	1.12	0.12	7	-	-	-	-
1050st1h	71.64	0.47	15.11	2.24	0.22	0.92	4.03	4.16	1.11	0.10	6	-	-	-	-
1050stdec100	71.39	0.52	15.19	2.11	0.20	0.95	4.12	4.24	1.16	0.11	6	-	-	-	-
1050stdec20	71.27	0.43	14.97	2.84	0.18	0.98	3.78	4.22	1.24	0.09	6	-	-	46–53	11
1050stdec5	75.90	0.60	12.27	2.63	0.17	0.71	2.05	4.04	1.52	0.11	7	-	-	50–55	14
970st	72.89	0.46	14.49	2.01	0.22	0.99	3.52	4.22	1.20	0.07	8	57–67	18	-	-
970st1h	74.13	0.52	13.76	2.01	0.15	0.96	3.09	4.09	1.28	0.07	10	55–65	10	-	-
970stdec100	73.84	0.36	13.59	2.49	0.18	1.00	3.07	4.25	1.23	0.08	5	52–65	13	46–61	12
970stdec20	73.64	0.55	13.79	2.47	0.13	0.96	3.10	4.02	1.30	0.03	7	48–63	8	50–65	12
970stdec5	75.25	0.49	13.00	2.54	0.13	0.57	2.38	4.13	1.43	0.09	8	51–64	18	48–64	20
940st	73.55	0.52	13.92	2.31	0.22	0.97	3.12	4.20	1.19	0.03	8	60–66	12	-	-
940st1h	73.33	0.39	13.86	2.79	0.15	0.85	3.07	4.24	1.27	0.05	10	61–68	14	-	-
940stdec100	74.51	0.56	13.40	2.16	0.19	0.81	2.78	4.19	1.31	0.09	7	61–65	11	59–70	30
940stdec20	75.69	0.49	12.94	2.57	0.12	0.49	2.35	3.80	1.44	0.10	7	49–64	10	48–72	18
940stdec5	76.57	0.58	12.49	2.02	0.18	0.38	1.98	4.17	1.54	0.09	7	51–65	13	52–63	17
940steq	79.13	0.38	11.42	1.69	0.04	0.24	0.90	3.69	2.33	0.17	3	54–67	10	51–67	23
900st	73.32	0.48	13.85	3.34	0.14	0.66	3.02	3.96	1.23	0.04	6	46–62	8	-	-
900st1h	72.89	0.48	13.76	3.56	0.12	0.68	3.07	4.14	1.28	0.01	7	54–64	8	-	-
900stdec100	74.66	0.52	13.22	3.20	0.15	0.68	2.52	3.69	1.37	0.00	6	57–69	8	50–72	21
900stdec20	76.84	0.48	12.18	2.61	0.22	0.54	2.01	3.61	1.47	0.04	7	54–64	13	50–64	17
900stdec5	77.50	0.48	11.74	2.70	0.11	0.36	1.68	3.82	1.51	0.10	7	54–63	10	52–79	23

[a] The number of analyses.

[b] "An_{rim}" and "An_{tiny}" represent the anorthite contents of plagioclase rim and tiny plagioclase, respectively.

Figure 1

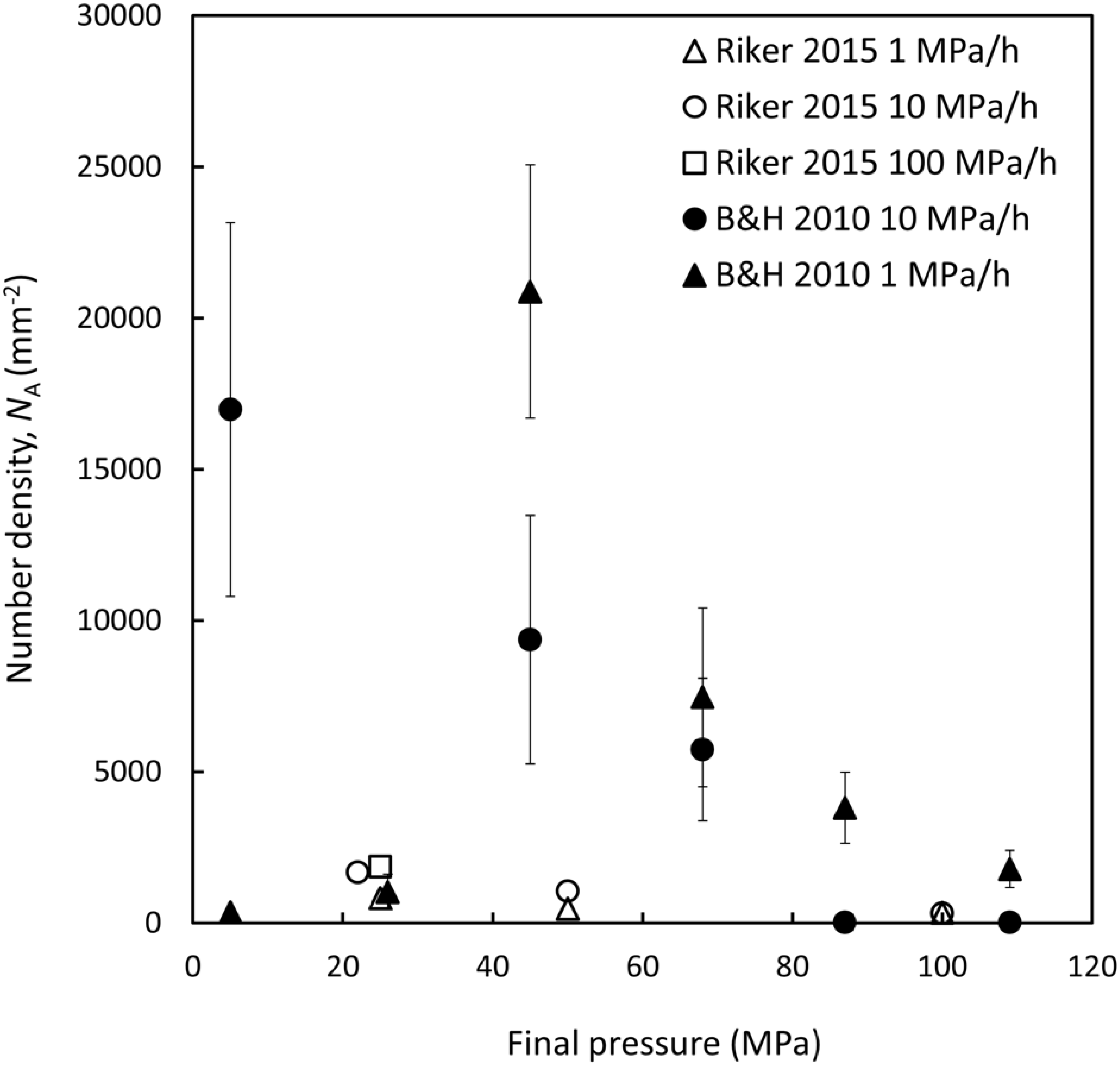
△ Riker 2015 1 MPa/h
○ Riker 2015 10 MPa/h
□ Riker 2015 100 MPa/h
● B&H 2010 10 MPa/h
▲ B&H 2010 1 MPa/h
Number density, N_A (mm^{-2})
30000
25000
20000
15000
10000
5000
0
0
20
40
60
80
100
120
Final pressure (MPa)

Figure 2

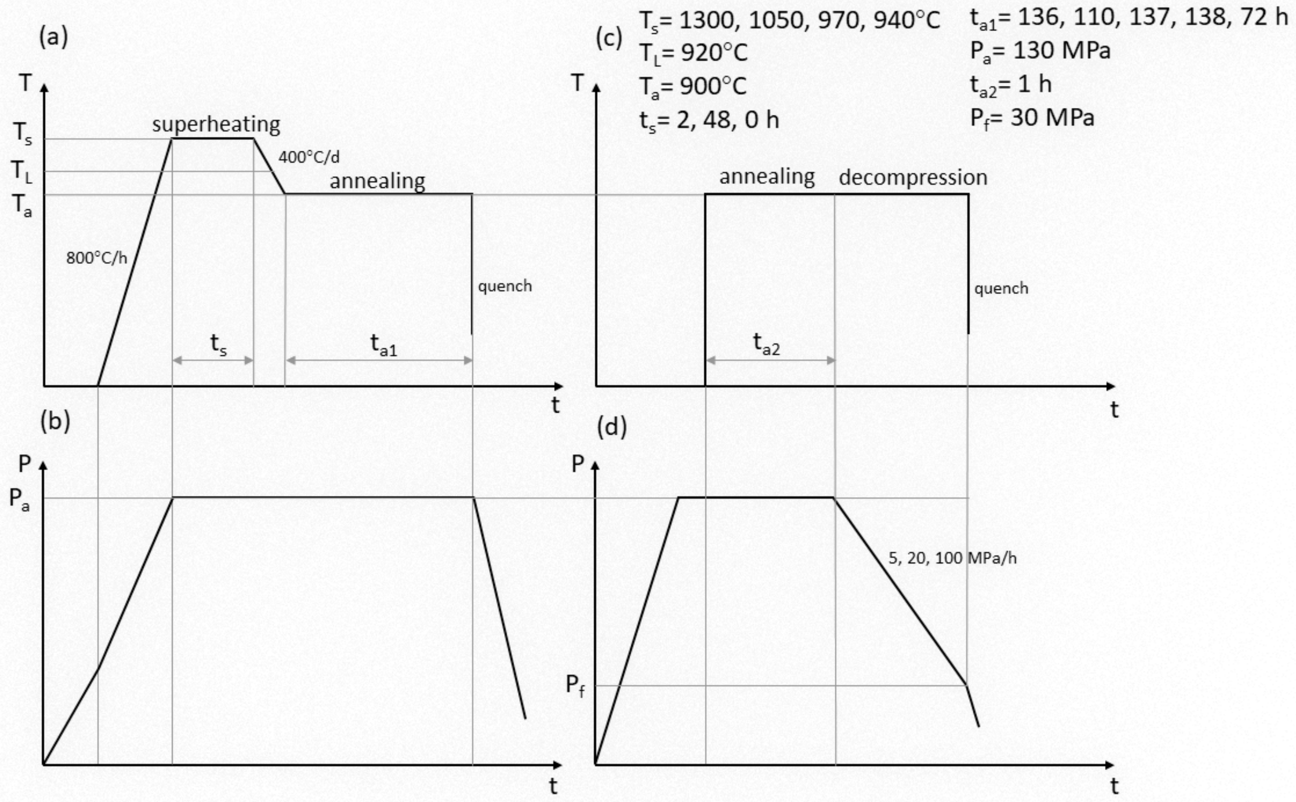
(a)
T
T_s
T_L
T_a
superheating
400°C/d
annealing
800°C/h
quench
t_s
t_{a1}
t
(b)
P
P_a
t
(c)
T_s= 1300, 1050, 970, 940°C
T_L= 920°C
T_a= 900°C
t_s= 2, 48, 0 h
t_{a1}= 136, 110, 137, 138, 72 h
P_a= 130 MPa
t_{a2}= 1 h
P_f= 30 MPa
T
annealing
decompression
quench
t_{a2}
t
(d)
P
5, 20, 100 MPa/h
P_f
t

Figure 3

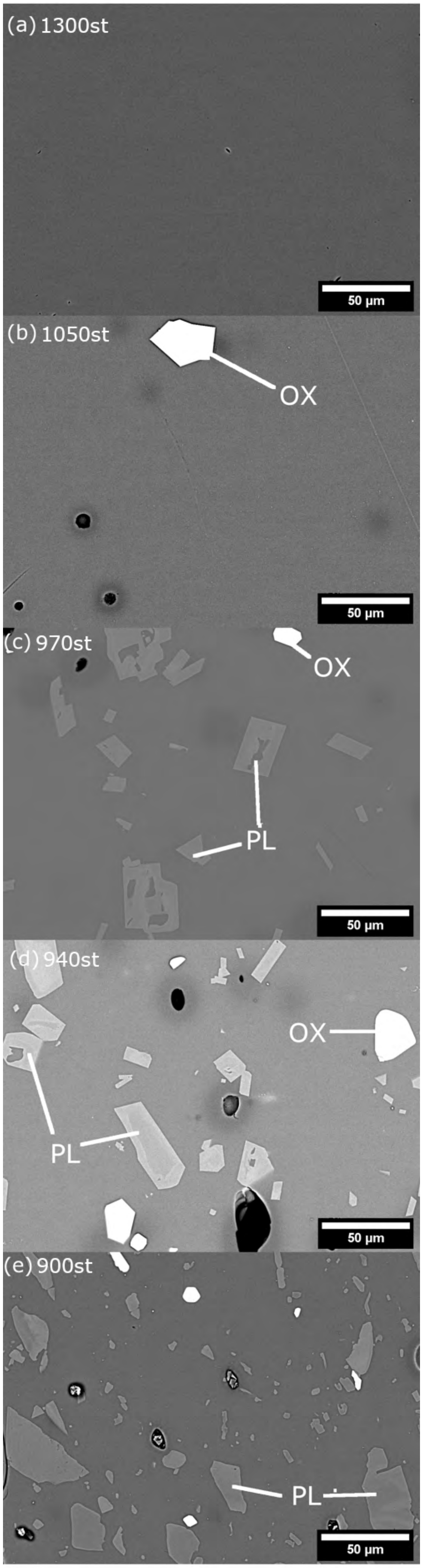
(a) 1300st
50 μm
(b) 1050st
OX
50 μm
(c) 970st
OX
PL
50 μm
(d) 940st
OX
PL
50 μm
(e) 900st
PL
50 μm

Figure 1

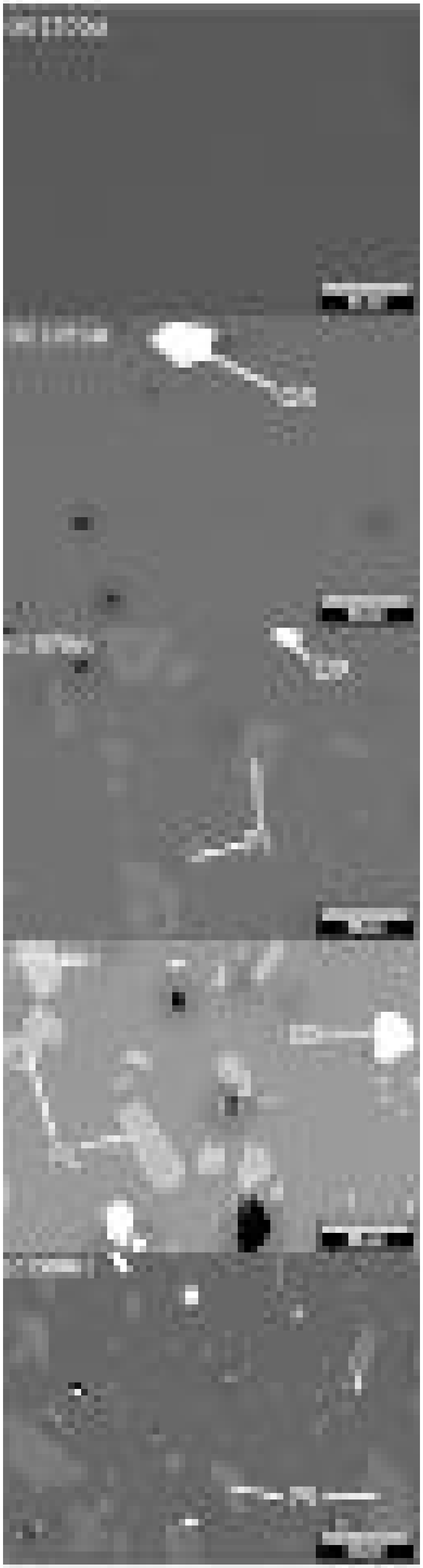

Figure 4

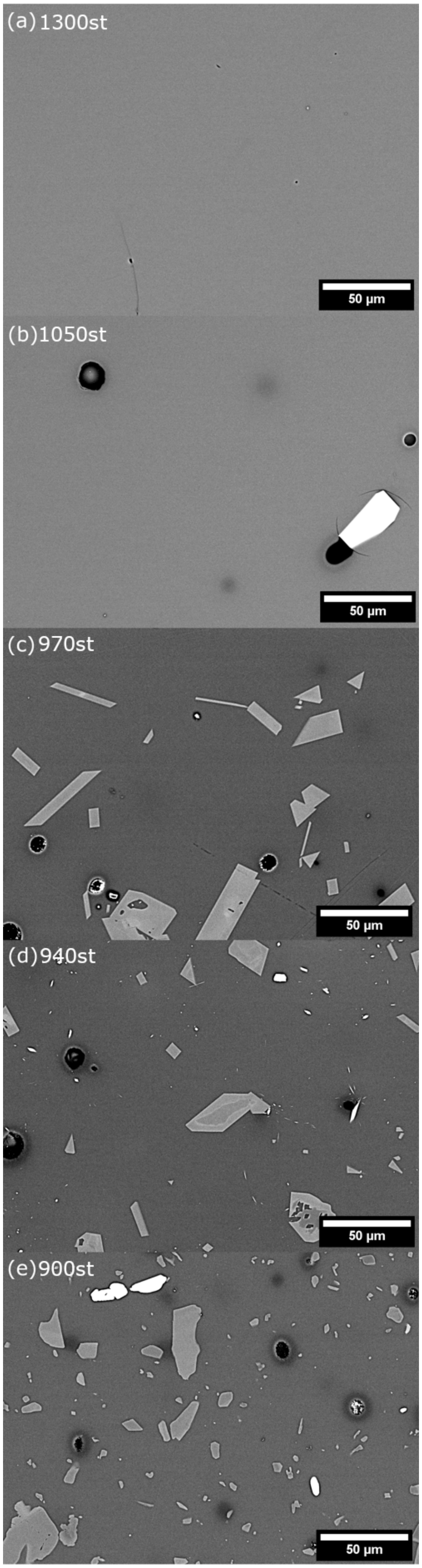
(a) 1300st
50 μm
(b)1050st
50 μm
(c) 970st
50 μm
(d)940st
50 μm
(e)900st
50 μm

Figure 4

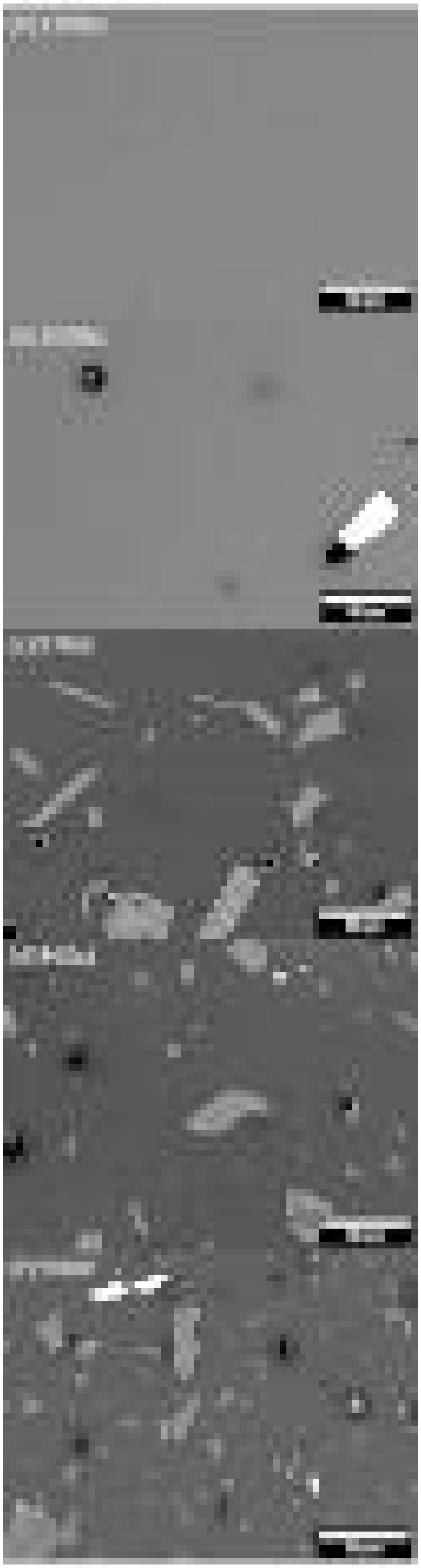

Figure 5

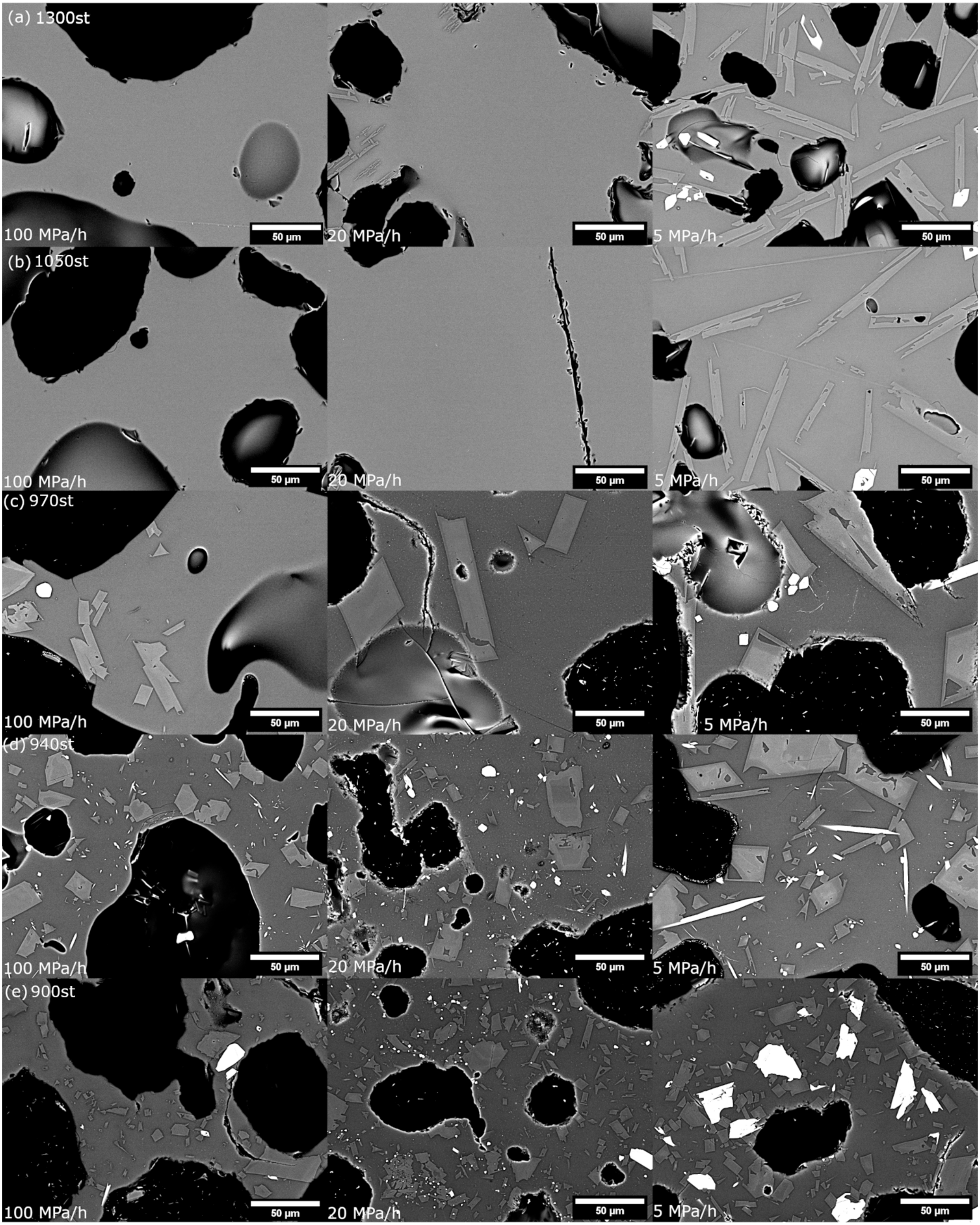
(a) 1300st
100 MPa/h
50 µm
20 MPa/h
50 µm
5 MPa/h
50 µm
(b) 1050st
100 MPa/h
50 µm
20 MPa/h
50 µm
5 MPa/h
50 µm
(c) 970st
100 MPa/h
50 µm
20 MPa/h
50 µm
5 MPa/h
50 µm
(d) 940st
100 MPa/h
50 µm
20 MPa/h
50 µm
5 MPa/h
50 µm
(e) 900st
100 MPa/h
50 µm
20 MPa/h
50 µm
5 MPa/h
50 µm

Figure 6

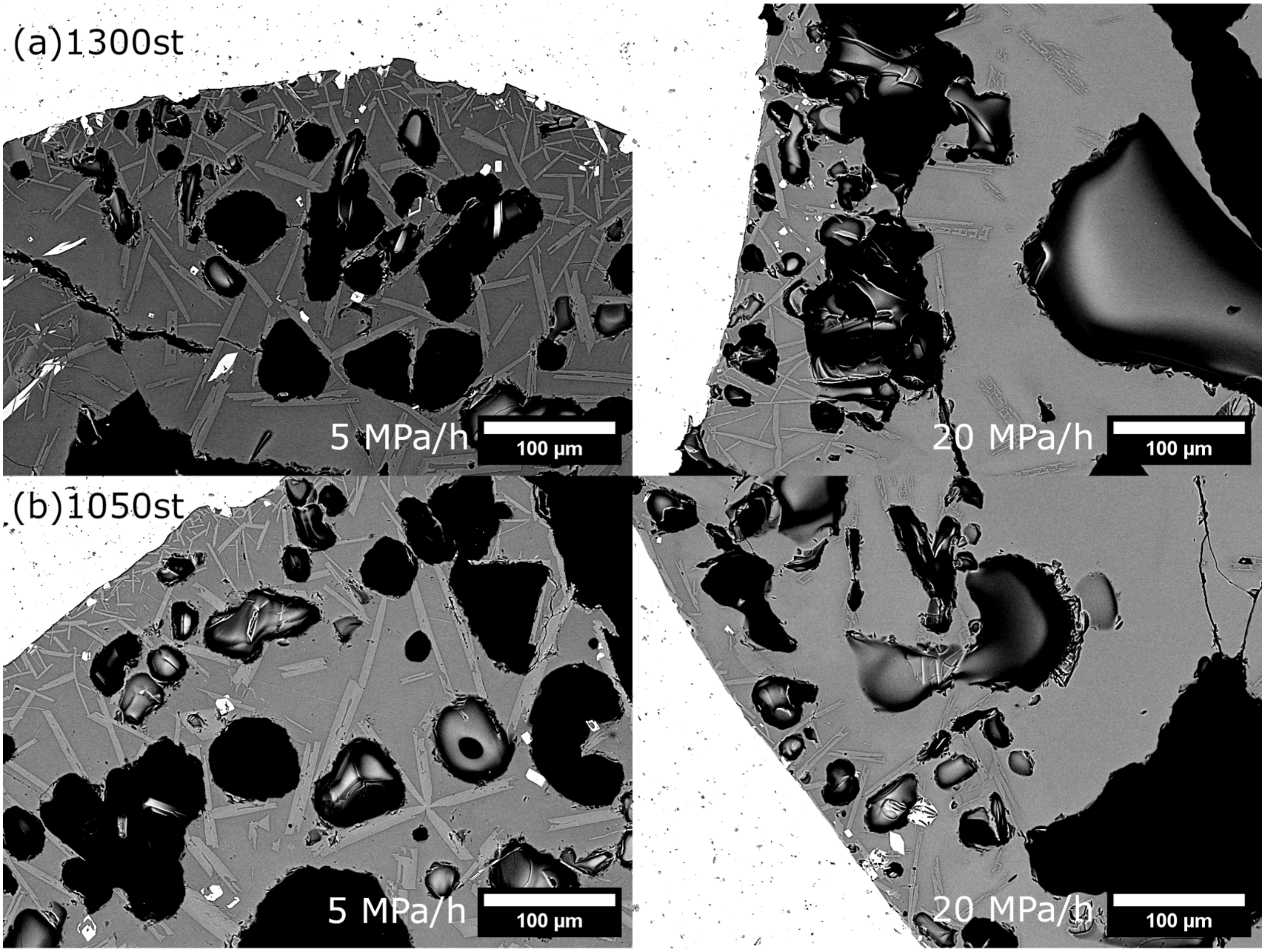
(a)1300st
5 MPa/h
100 µm
20 MPa/h
100 µm
(b)1050st
5 MPa/h
100 µm
20 MPa/h
100 µm

Figure 7

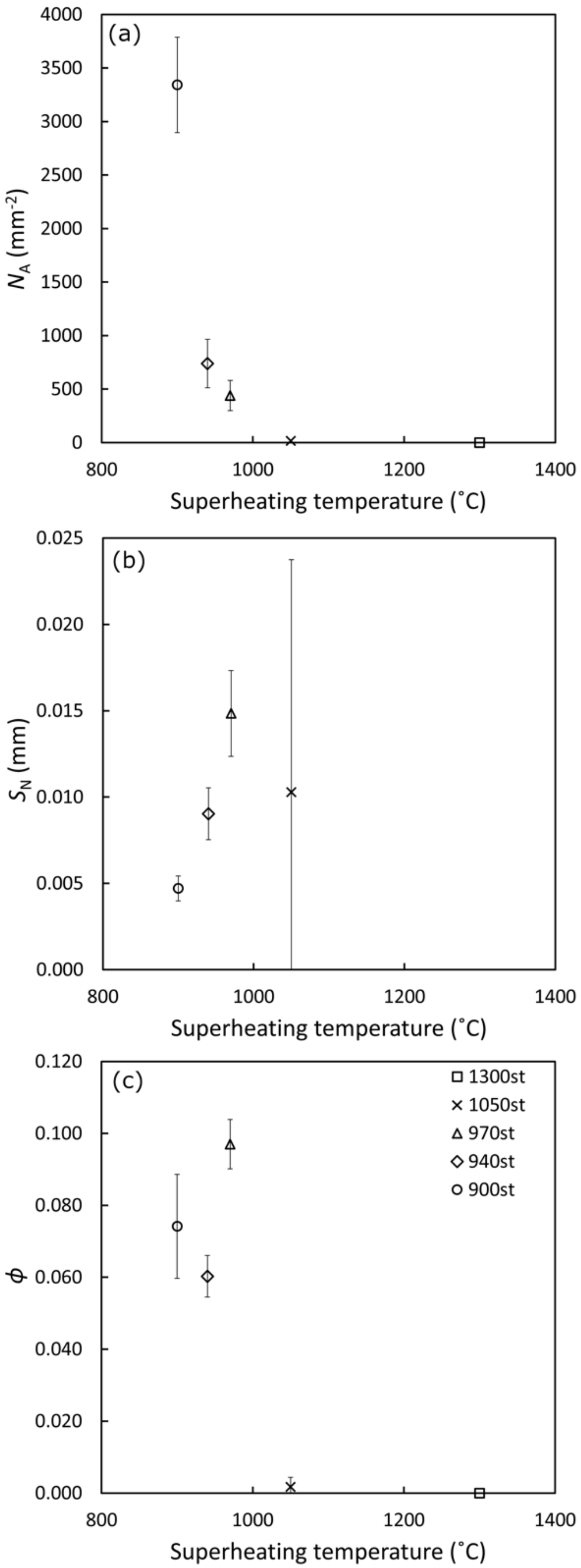
(a)
4000
3500
3000
2500
2000
1500
1000
500
0
N_A (mm^{-2})
800
1000
1200
1400
Superheating temperature (˚C)
(b)
0.025
0.020
0.015
0.010
0.005
0.000
S_N (mm)
800
1000
1200
1400
Superheating temperature (˚C)
(c)
0.120
0.100
0.080
0.060
0.040
0.020
0.000
ϕ
800
1000
1200
1400
Superheating temperature (˚C)
□ 1300st
× 1050st
△ 970st
◇ 940st
○ 900st

Figure 8

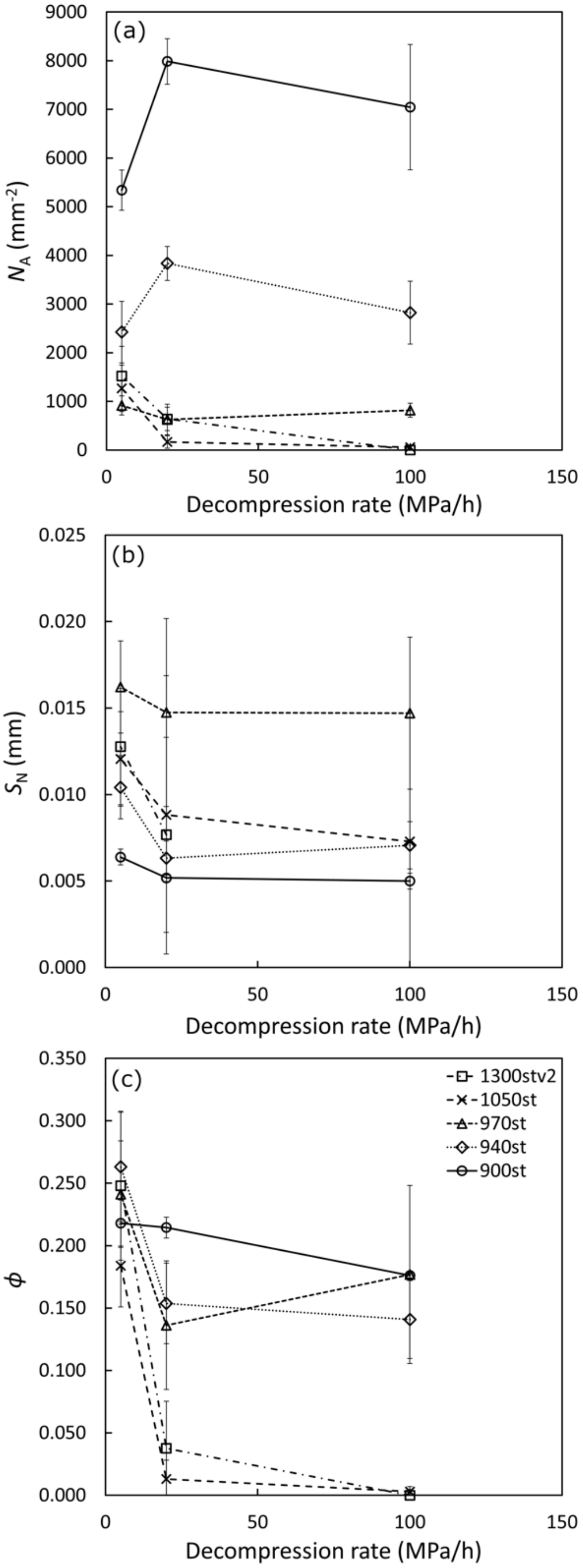
(a)
N_A (mm^{-2})
9000
8000
7000
6000
5000
4000
3000
2000
1000
0
0
50
100
150
Decompression rate (MPa/h)
(b)
S_N (mm)
0.025
0.020
0.015
0.010
0.005
0.000
0
50
100
150
Decompression rate (MPa/h)
(c)
ϕ
0.350
0.300
0.250
0.200
0.150
0.100
0.050
0.000
0
50
100
150
Decompression rate (MPa/h)
1300stv2
1050st
970st
940st
900st

Figure 9

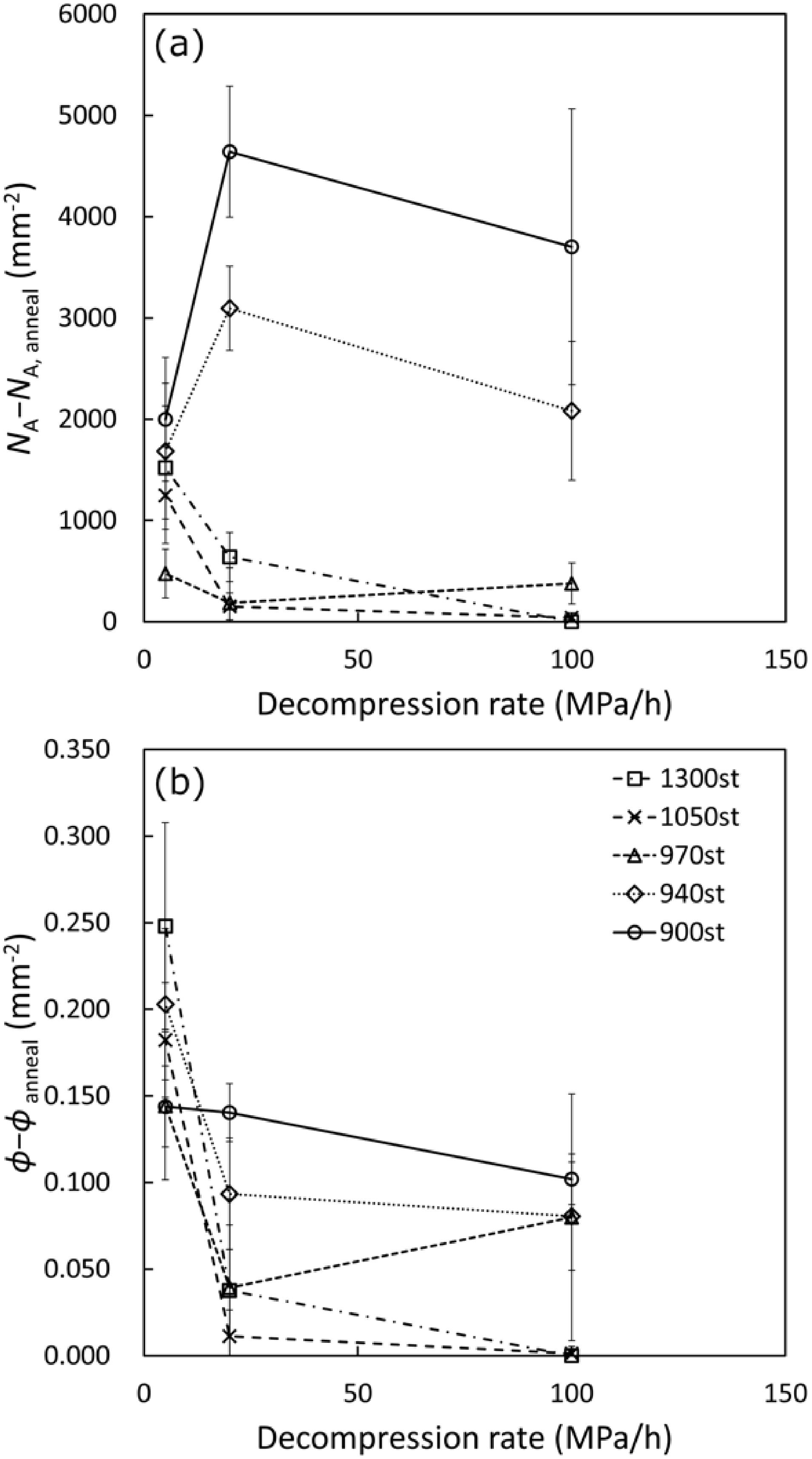
(a)
6000
5000
4000
3000
2000
1000
0
$N_A - N_{A,\text{ anneal}}$ (mm^{-2})
0
50
100
150
Decompression rate (MPa/h)
(b)
0.350
0.300
0.250
0.200
0.150
0.100
0.050
0.000
$\phi - \phi_{\text{anneal}}$ (mm^{-2})
1300st
1050st
970st
940st
900st
0
50
100
150
Decompression rate (MPa/h)

Figure 10

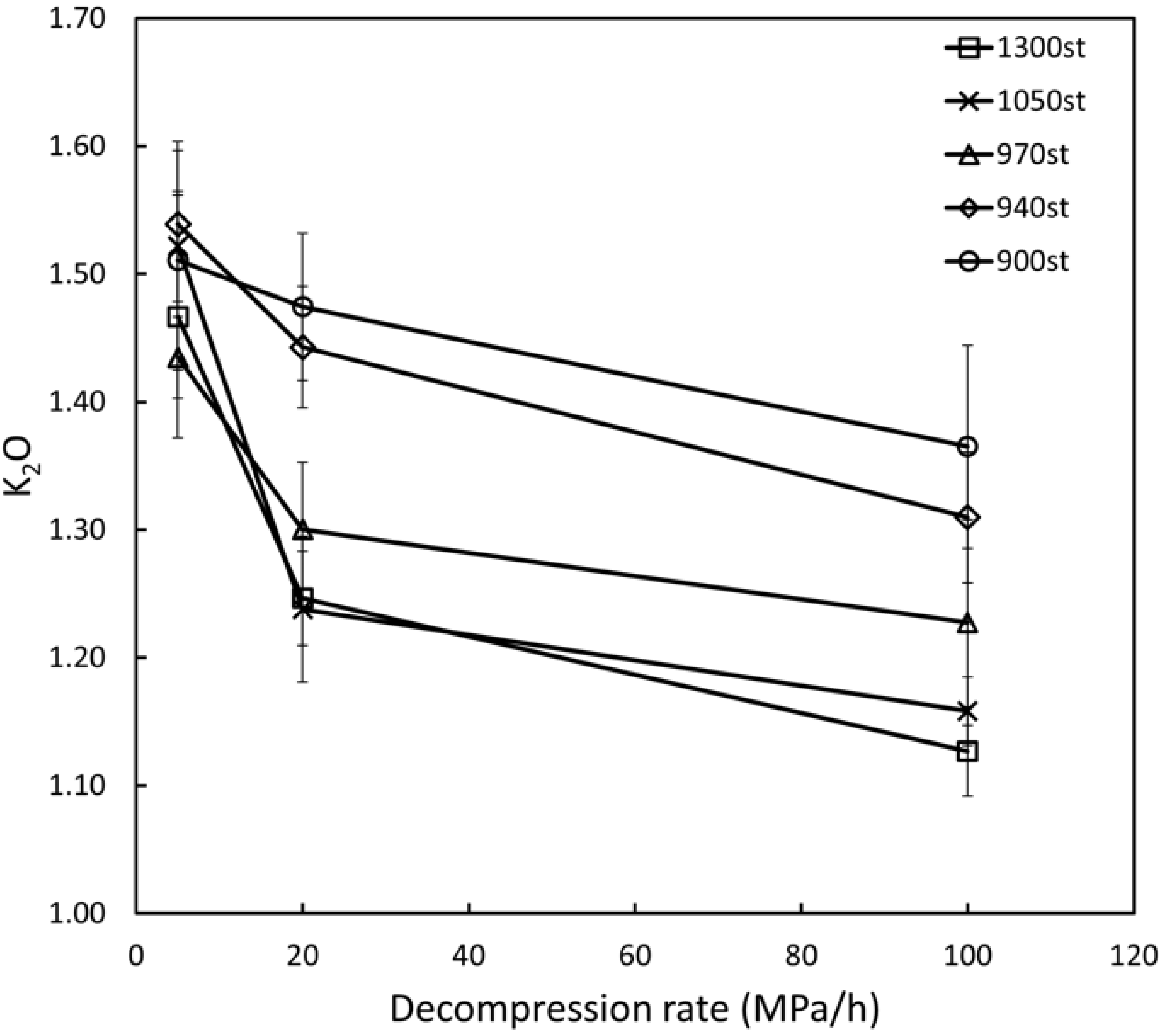
1.70
1.60
1.50
1.40
1.30
1.20
1.10
1.00
K_2O
0
20
40
60
80
100
120
Decompression rate (MPa/h)
1300st
1050st
970st
940st
900st

Figure 11

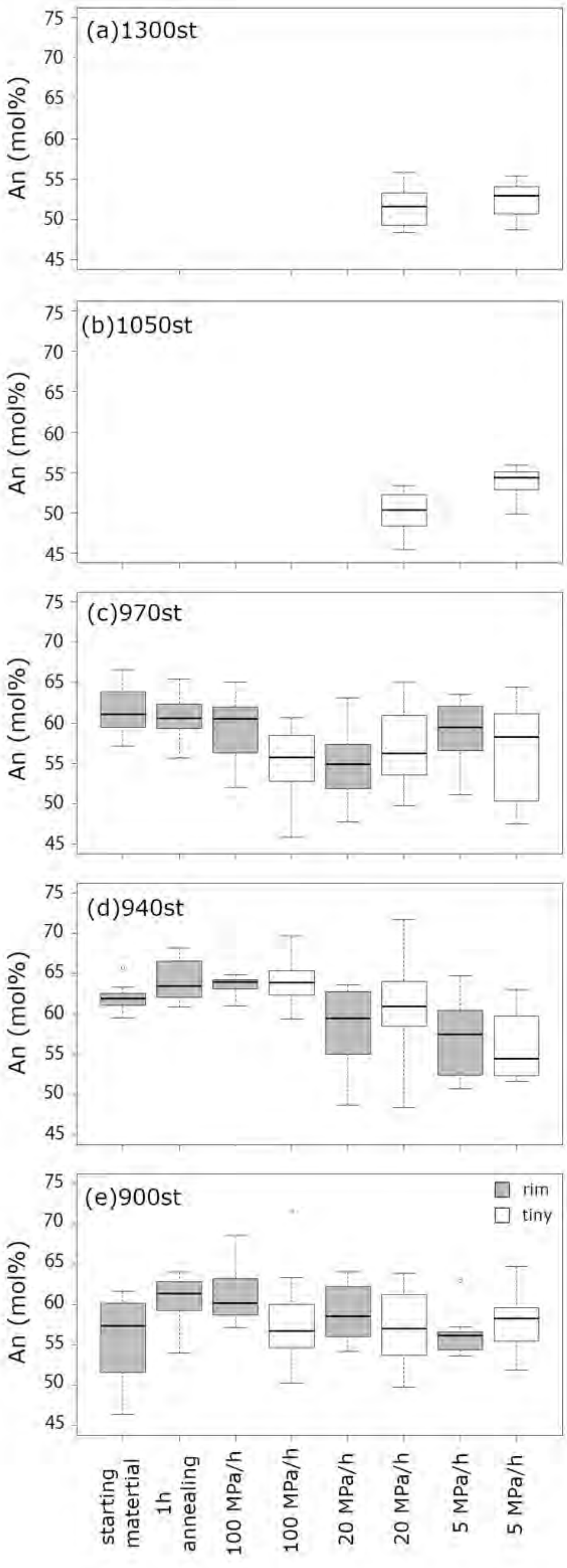
(a)1300st
(b)1050st
(c)970st
(d)940st
(e)900st
An (mol%)
75
70
65
60
55
50
45
▨ rim
☐ tiny
starting matertial
1h annealing
100 MPa/h
100 MPa/h
20 MPa/h
20 MPa/h
5 MPa/h
5 MPa/h

Figure 12

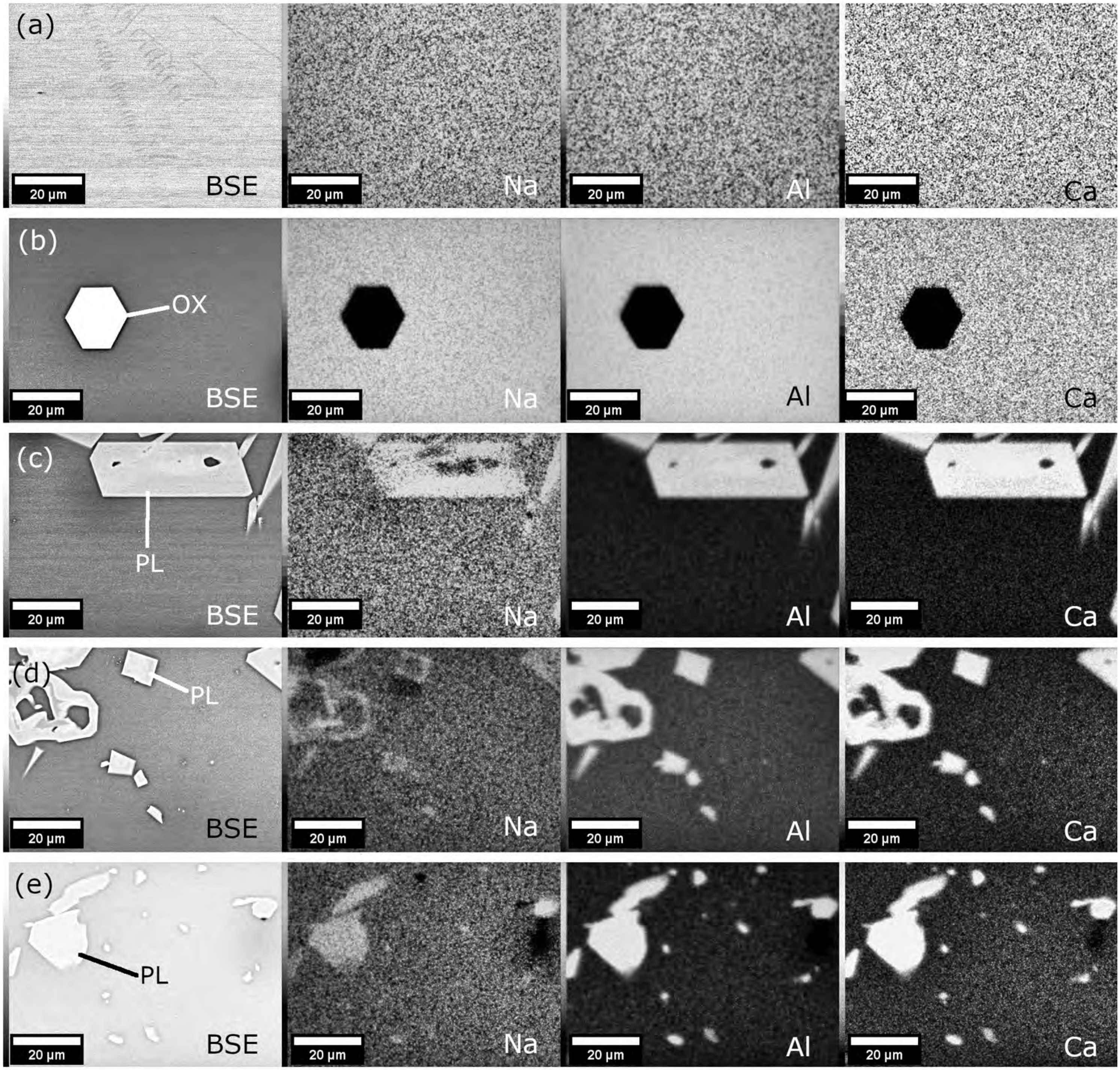

Figure 13

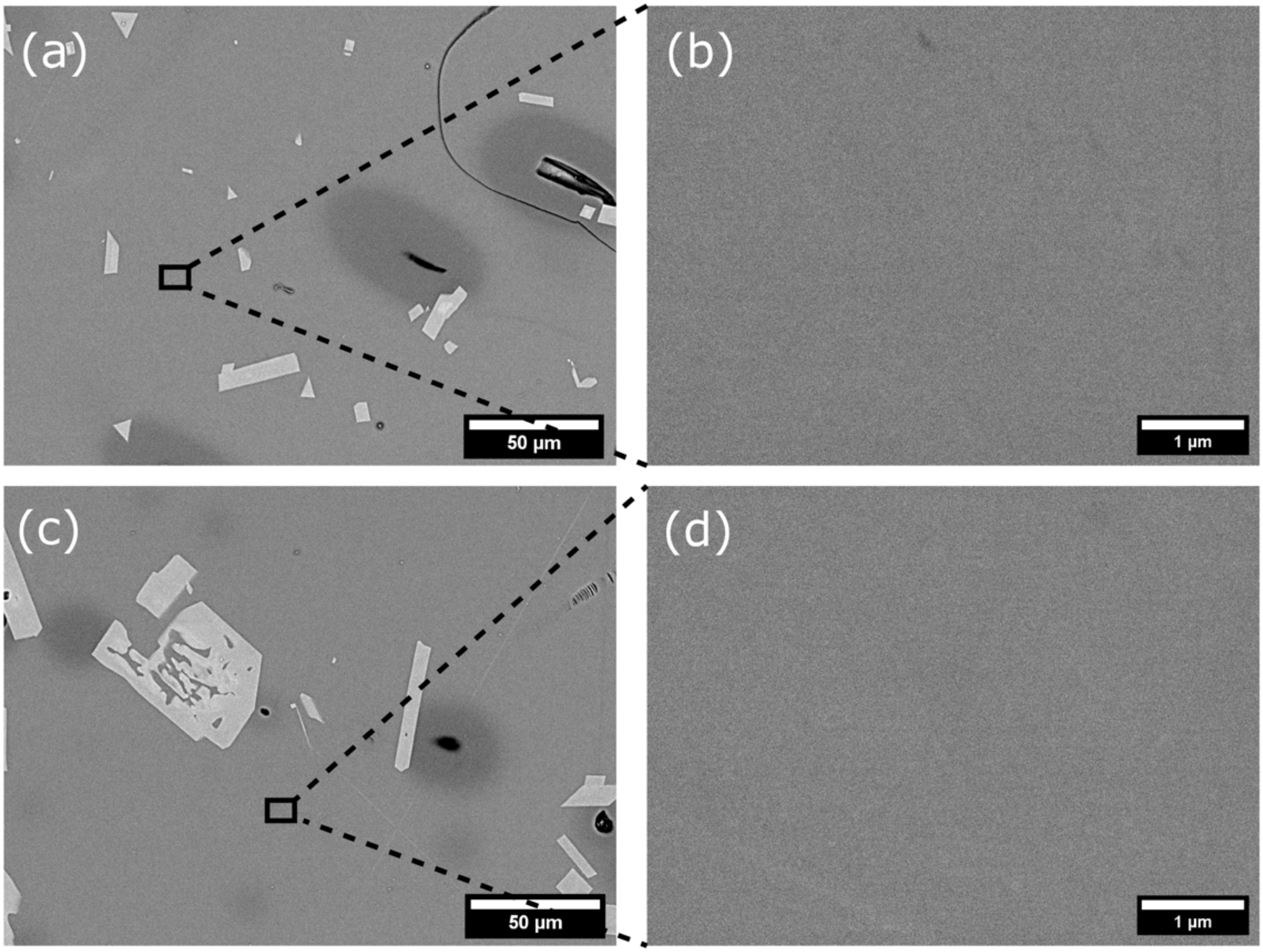

Figure 14

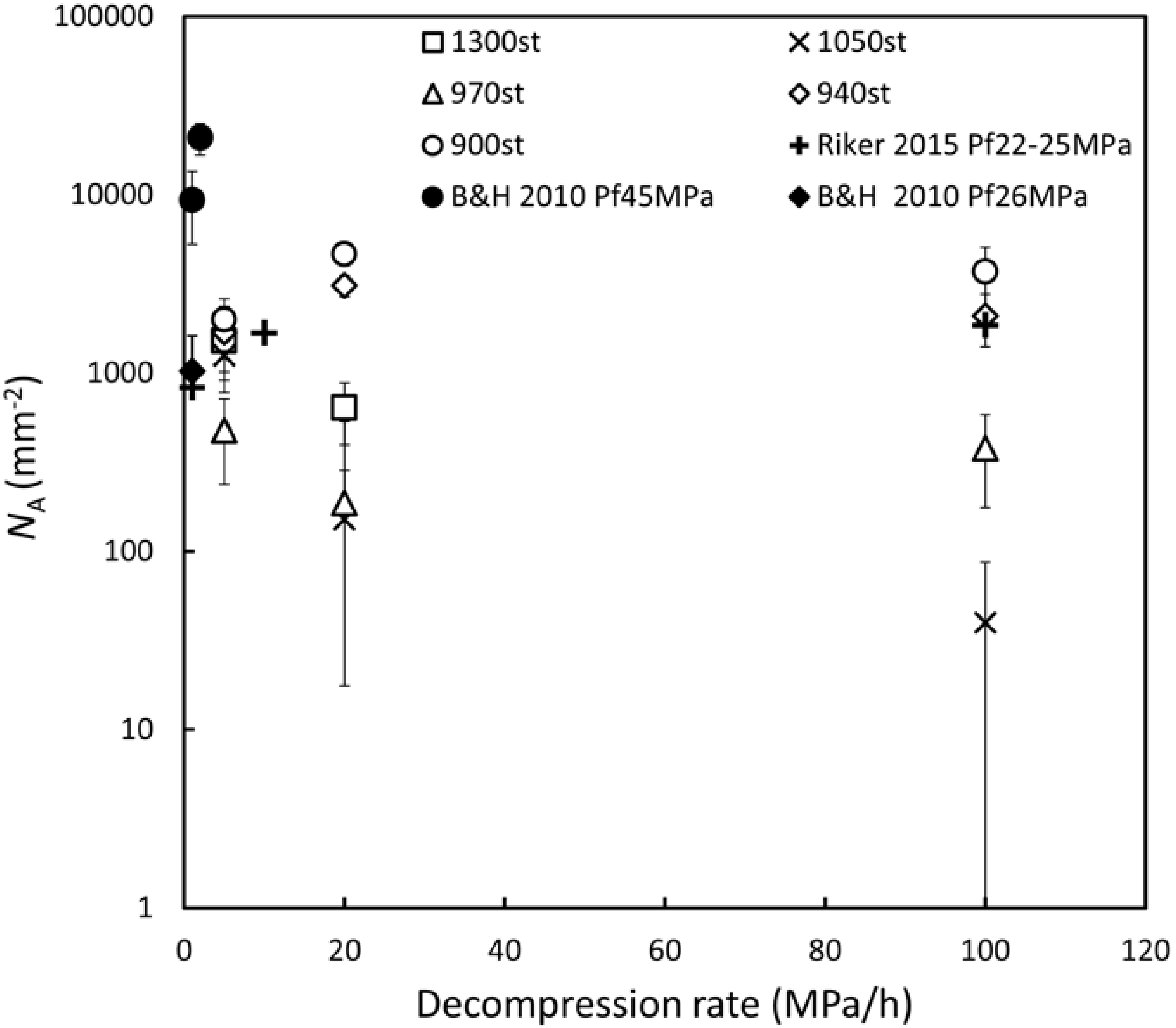
□ 1300st
× 1050st
△ 970st
◇ 940st
○ 900st
✚ Riker 2015 Pf22-25MPa
● B&H 2010 Pf45MPa
◆ B&H 2010 Pf26MPa
N_A (mm^{-2})
100000
10000
1000
100
10
1
0
20
40
60
80
100
120
Decompression rate (MPa/h)